

Density profile of dark matter haloes and galaxies in the Horizon-AGN simulation: the impact of AGN feedback

Sébastien Peirani^{1,2,3*}, Yohan Dubois¹, Marta Volonteri¹, Julien Devriendt^{4,5}, Kevin Bundy², Joe Silk^{1,4,6}, Christophe Pichon^{1,7}, Sugata Kaviraj⁸, Raphaël Gavazzi¹ and Mélanie Habouzit^{1,9}

¹ Institut d’Astrophysique de Paris (UMR 7095: CNRS & UPMC), 98 bis Bd Arago, 75014 Paris, France

² Kavli IPMU (WPI), UTIAS, The University of Tokyo, Kashiwa, Chiba 277-8583, Japan

³ Department of Physics, The University of Tokyo, Tokyo 113-0033, Japan

⁴ Sub-department of Astrophysics, University of Oxford, Keble Road, Oxford OX1 3RH

⁵ Observatoire de Lyon, UMR 5574, 9 avenue Charles André, Saint Genis Laval 69561, France

⁶ Department of Physics and Astronomy, The Johns Hopkins University Homewood Campus, Baltimore, MD 21218, USA

⁷ Korea Institute of Advanced Studies (KIAS) 85 Hoegiro, Dongdaemun-gu, Seoul, 02455, Republic of Korea

⁸ Centre for Astrophysics Research, University of Hertfordshire, College Lane, Hatfield, Herts, AL10 9AB, UK

⁹ Center for Computational Astrophysics CCA, 160 5th Ave New York

15 December 2018

ABSTRACT

Using a suite of three large cosmological hydrodynamical simulations, HORIZON-AGN, HORIZON-NOAGN (no AGN feedback) and HORIZON-DM (no baryons), we investigate how a typical sub-grid model for AGN feedback affects the evolution of the inner density profiles of massive dark matter haloes and galaxies. Based on direct object-to-object comparisons, we find that the integrated inner mass and density slope differences between objects formed in these three simulations (hereafter, H_{AGN} , H_{noAGN} and H_{DM}) significantly evolve with time. More specifically, at high redshift ($z \sim 5$), the mean central density profiles of H_{AGN} and H_{noAGN} dark matter haloes tend to be much steeper than their H_{DM} counterparts owing to the rapidly growing baryonic component and ensuing adiabatic contraction. By $z \sim 1.5$, these mean halo density profiles in H_{AGN} have flattened, pummelled by powerful AGN activity (“quasar mode”): the integrated inner mass difference gaps with H_{noAGN} haloes have widened, and those with H_{DM} haloes have narrowed. Fast forward 9.5 billion years, down to $z = 0$, and the trend reverses: H_{AGN} halo mean density profiles drift back to a more cusped shape as AGN feedback efficiency dwindles (“radio mode”), and the gaps in integrated central mass difference with H_{noAGN} and H_{DM} close and broaden respectively. On the galaxy side, the story differs noticeably. Averaged stellar profile central densities and inner slopes are monotonically reduced by AGN activity as a function of cosmic time, resulting in better agreement with local observations. As both dark matter and stellar inner density profiles respond quite sensitively to the presence of a central AGN, there is hope that future observational determinations of these quantities can be used constrain AGN feedback models.

Key words: galaxies: evolution – galaxies: haloes – galaxies: jets – dark matter – Methods: numerical

1 INTRODUCTION

The inner structure of dark matter haloes represents one of the most important constraint on cosmological and galaxy formation models. Within the cold dark matter (CDM) paradigm,

* E-mail: peirani@iap.fr

earlier works ignoring the effects of gas dissipation and star formation processes, have suggested that dark matter haloes have spherically-averaged density profiles that can be well fitted by simple analytical function such as the NFW profile (Navarro et al. 1996a; Navarro et al. 1997) in which the inner slope tends to -1 or could even be as steep as -1.5 (e.g. Moore et al. 1998; Jing & Suto 2000). Later numerical works favour the Einasto profile with a finite central density though this profile is still cuspy and close to the NFW one (Merritt et al. 2006; Stadel et al. 2009; Navarro et al. 2010).

The prediction of a peaked inner density profile seems to be seriously challenged by observations. In particular, dwarfs and low surface-brightness galaxies suggest a much shallower profile with a relatively flat slope ($\alpha \geq -0.5$ with $\rho(r) \sim r^\alpha$) (Palunas & Williams 2000; Salucci & Burkert 2000; de Blok et al. 2001; Swaters et al. 2003; Gentile et al. 2004; Spekkens et al. 2005; Goerdt et al. 2006; Walter et al. 2008; de Blok et al. 2008; Oh et al. 2011; Walker & Peñarrubia 2011). On the other extreme of the halo mass scale, galaxy clusters tend to have a central cusp, as evidenced by studies combining strong and weak lensing (e.g., Limousin et al. 2007; Leonard et al. 2007; Umetsu et al. 2007), but shallower slopes than the NFW one can also be found within the inner ≈ 5 kpc (Sand et al. 2004; Sand et al. 2008; Newman et al. 2009; Newman et al. 2011; Newman et al. 2013; Richtler et al. 2011). Note that a recent study found a cusp slope over $5 - 350$ kpc of $\alpha = -1.62$, again from combined weak and strong lensing analysis of the complete CLASH cluster sample (Zitrin et al. 2015).

This so-called ‘‘cusp-core problem’’ could imply that the CDM paradigm needs to be revised to account for dark matter self-interaction (Yoshida et al. 2000; Burkert 2000; Kochanek & White 2000; Spergel & Steinhardt 2000; Davé et al. 2001; Ahn & Shapiro 2005; Vogelsberger et al. 2014, Elbert et al. 2015; Lin & Loeb 2016), a warmer dark matter candidate (Colín et al. 2000; Bode et al. 2001, Lovell et al. 2012) or an ultralight axion-particle (e.g., Marsh & Pop 2015), and/or a more exotic coupling between dark matter and dark energy (e.g. Macciò et al. 2015). Alternatively, it could simply mean that baryonic processes play a key role in shaping the inner parts of halos and galaxies. Indeed, several astrophysical solutions have been proposed to reconcile observations with theoretical predictions. Stellar feedback could produce rapid variations of the gravitational potential through substantial gas mass outflows from the central region. This would flatten the inner density profile of the dark matter halo (Navarro et al. 1996b; Gnedin & Zhao 2002; Read & Gilmore 2005; Mashchenko et al. 2006, 2008; Ogiya & Mori 2011, 2014; Governato et al. 2012; Pontzen & Governato 2012; Macciò et al. 2012; Teyssier et al. 2013; Oñorbe et al. 2015; Chan et al. 2015; El-Zant et al. 2016; Del Popolo & Pace 2016). On the other hand, dark matter can also be gravitationally ‘‘heated’’ by baryons through dynamical friction caused either by self-gravitating gas clouds orbiting near the center of the galaxy (El-Zant et al. 2001, El-Zant et al. 2004; Jardel & Sellwood 2009; Lackner & Ostriker 2010; Cole et al. 2011, Del Popolo & Pace 2016) by the presence of a stellar bar (Weinberg & Katz 2002; Holley-Bockelmann et al. 2005; Sellwood 2008), by the radiation recoil from coalescing black holes (Merritt et al. 2004), or by processes which transfer of angular momentum from baryons to dark matter (Tonini et al. 2006, Del Popolo 2009).

On larger mass scales, numerical simulations from

Peirani et al. (2008) (see also Duffy et al. 2010; Dubois et al. 2010; Teyssier et al. 2011; Martizzi et al. 2012, 2013) have argued that active galactic nuclei (AGN) feedback plays a similar role to that of stellar feedback in smaller systems: it can heat/expel large amounts of gas from the central regions of galaxy groups and clusters. A fraction of this gas then cools and returns to the centre, generating repeated cycles of significant inflows/outflows which in turn cause rapid fluctuations of the gravitational potential, steepening/flattening out the inner dark matter halo and galaxy stellar density profiles. Such a mechanism is commonly invoked to explain the substantial body of observational evidence that the majority of massive elliptical or cD galaxies exhibit very shallow slopes in their inner (≈ 1 kpc) stellar surface brightness profiles (Kormendy 1999; Quillen, Bower & Stritzinger 2000; Laine et al. 2003; Graham 2004; Trujillo et al. 2004; Lauer et al. 2005; Ferrarese et al. 2006; Côté et al. 2007; Kormendy et al. 2009; Graham 2013). A related phenomenon is the formation of cores within the central 100 pc of massive ellipticals. These are believed to be formed dynamically, by the scouring effect of possibly stalled supermassive black hole (SMBH) binaries at ~ 10 pc separation (see for instance Faber et al. 1997; Thomas et al. 2014 and references therein). Larger cores are also found, for more widely separated SMBH pairs, of up to ~ 500 pc extent (e.g. Mazzalay et al. 2016 and references therein).

In the present paper, we aim to extend previous theoretical work on the role played by AGN feedback, using a statistically representative sample spanning a comprehensive range of dark matter halo and galaxies masses and looking at the evolution of their inner density profiles throughout a considerable fraction of the age of the Universe. This sample is extracted from our state-of-the-art hydrodynamical cosmological simulation HORIZON-AGN (Dubois et al. 2014) which includes gas cooling, star formation, stellar and AGN feedback, and that we compare with two other simulations HORIZON-NOAGN (no AGN feedback) and HORIZON-DM (no baryons) stripped down in terms of modelled physical processes but featuring identical initial conditions. These simulations have been used to highlight the role of AGN feedback (Volonteri et al. 2016) in regulating the baryon content of massive galaxies (Kaviraj et al. 2016; Beckmann et al. 2016) and their morphological transformations (Welker et al. 2015; Dubois et al. 2016).

The paper is organized as follows. Section 2 briefly summarises the numerical modelling upon which this work is based (simulations and post-processing). Section 3 and 4 present our main results concerning the evolution of the inner density profiles of massive dark matter haloes and galaxies respectively. Finally, we put forward and discuss our conclusions in Section 5.

2 NUMERICAL MODELLING

2.1 The three simulations H_{AGN} , H_{noAGN} , and H_{DM}

In this paper, we analyse and compare two large cosmological hydrodynamical simulations, HORIZON-AGN (H_{AGN}), HORIZON-NOAGN (H_{noAGN}) and one dark matter only cosmological simulation HORIZON-DM (H_{DM}). HORIZON-AGN is already described in Dubois et al. (2014), so we only summarise here its main features. We adopt a standard Λ CDM cosmology with total matter density $\Omega_{\text{m}} = 0.272$, dark energy density $\Omega_{\Lambda} = 0.728$, amplitude of the matter power

spectrum $\sigma_8 = 0.81$, baryon density $\Omega_b = 0.045$, Hubble constant $H_0 = 70.4 \text{ km s}^{-1} \text{ Mpc}^{-1}$, and $n_s = 0.967$ compatible with the WMAP-7. The size of the simulated volume is $L_{\text{box}} = 100 h^{-1} \text{ Mpc}$ on a side, and it contains 1024^3 dark matter (DM) particles, which results in a DM mass resolution of $M_{\text{DM, res}} = 8.27 \times 10^7 M_\odot$. The simulation is run with the RAMSES code (Teyssier 2002), and the initially uniform grid is adaptively refined down to $\Delta x = 1$ proper kpc at all times. Refinement is triggered in a quasi-Lagrangian manner: if the number of DM particles becomes greater than 8, or the total baryonic mass reaches 8 times the initial DM mass resolution in a cell.

Gas can radiatively cool down to 10^4 K through H and He collisions with a contribution from metals using rates tabulated by Sutherland & Dopita (1993). Heating from a uniform UV background takes place after redshift $z_{\text{reion}} = 10$ following Haardt & Madau (1996). The star formation process is modelled using a Schmidt law: $\dot{\rho}_* = \epsilon_* \rho / t_{\text{ff}}$ for gas number density above $n_0 = 0.1 \text{ H cm}^{-3}$, where $\dot{\rho}_*$ is the star formation rate density, $\epsilon_* = 0.02$ the constant star formation efficiency, and t_{ff} the local free-fall time of the gas. The stellar mass resolution is $M_{*, \text{res}} = 2 \times 10^6 M_\odot$. Feedback from stellar winds, supernovae type Ia and type II are also taken into account for mass, energy and metal release (Kimm, 2012).

Black hole (BH) formation is also included, and BHs accrete gas at a Bondi-capped-at-Eddington rate and coalesce when they form a tight enough binary. They also release energy in a quasar (heating) or radio (kinetic jet) mode when the accretion rate is above (below) one per cent of Eddington, with efficiencies tuned to match the BH-galaxy scaling relations (see Dubois et al. 2012 for detail). The presence of both quasar and radio modes is supported by recent observations. In particular, using MaNGA data (Bundy et al. 2015), Cheung et al. (2016) report the presence of bi-symmetric emission features in the centre of quiescent galaxies of mass around $2 \times 10^{10} M_\odot$ from which they infer the presence of centrally driven winds. On top of the fact that such “red geysers” galaxies seem to be very common at this mass scale (Bundy et al., in prep), the energy released by their SMBHs is capable of driving the observed winds and displays a mechanical content sufficient to suppress star formation. It is therefore very likely that such kinetic winds (radio mode) play a crucial role in galaxy formation and should be taken into account in numerical models (see for instance, Weinberger et al. 2016).

HORIZON-NOAGN and HORIZON-DM were performed using the same set of initial conditions and sub-grid modelling of physical processes but with no BH formation (and therefore no AGN feedback) and baryons respectively.

2.2 Dark matter halo and galaxy catalogues

Dark matter haloes are identified using the ADAPTAHOP (sub)halo finder (Aubert et al. 2004, Tweed et al. 2009). In our different catalogues, host haloes and subhaloes are studied separately. Since we are particularly interested in studying the very inner part of dark matter haloes, a robust definition of their centre is critical. In general, the position of the most bound particle yields an accurate estimate, especially in the case of HORIZON-NOAGN and HORIZON-DM as haloes in these simulations have cuspy inner profiles. However, as far as HORIZON-AGN is concerned, as we will see in the remainder of this paper, the dark matter profiles of haloes hosting large

galaxies can be flatter. Therefore, for some (rare) object in this latter simulation, the centre can be associated with a substructure which is offset from the “real” centre of mass and could lead to the attribution of a spurious core. To circumvent this issue, we use a shrinking sphere approach (Power et al. 2003) whereby starting from the virial radius, we recursively identify the centre of mass within spheres 10% smaller in linear size at each iteration. We stop the procedure once the sphere reaches a 2 kpc radius and identify the centre of the halo with its densest particle. Twenty neighbours are used to compute the local density. Only structures with an average density larger than 200 times the average matter density and containing more than 100 particles become part of the (sub)halo catalogue.

Galaxies are also identified with ADAPTAHOP but applied to star particles. In this case, we use the most bound particle as the definition of the centre of mass and only galaxies with more than 50 star particles are part of the final catalogue.

Finally, we build the merger trees of all the dark matter haloes and galaxies for each simulation, using TREEMAKER (Tweed et al. 2009) to link 52 outputs equally spaced in time between $z \sim 5.8$ and $z = 0$, i.e. with a time resolution of $\sim 250 \text{ Myr}$.

These procedures yield, for the HORIZON-AGN run at redshift zero, about 250000 haloes and subhaloes with a mass greater than $10^{10} M_\odot$ and 125000 galaxies with a mass greater than $10^8 M_\odot$.

2.3 Matching dark matter haloes and galaxies

Since we start from the same initial conditions, each dark matter particle possesses an identity which is identical in any of the 3 simulations. Thus, if 75% or more of the particles of any given halo in the HORIZON-AGN run also belong to a halo identified in the HORIZON-NOAGN or HORIZON-DM runs, we initially assume that these haloes are twins. However, if the mass ratio of the matching pair is greater than 10 (or lower than 0.1), we exclude it from our comparison sample. This last step is rendered necessary because sub-structures can get their particles stripped by the host halo at different times and with different intensities in the three simulations. As a result, a subhalo could become twinned with a much more massive host halo if its equivalent subhalo in the other simulation has already been destroyed (or has become too small to be detected). In general, we are able to match more than 85% of dark matter objects at any redshift by applying these two criteria.

We cannot implement the same procedure for galaxies since a given stellar particle is not necessarily created at the exact same moment in the very same galaxy in HORIZON-AGN and HORIZON-NOAGN. Moreover, the total number of stellar particles will also differ as it depends on the impact AGN feedback has on the star formation process. Therefore, instead of relying upon a common identity of the stellar particles they are composed of to directly match objects between runs, we first couple each galaxy to a host dark matter halo in their parent simulation. We determine these galaxy-halo pairs by picking the most massive galaxy whose centre is located within a sphere of radius equal to 5% of the virial radius of its host halo. Galaxy twins between runs are then determined through the matching of their host halo as previously described.

To illustrate the typical efficiency of such a procedure, at $z = 0$, we are able to match about 68% of H_{AGN} galaxies with

a mass greater $10^{10}M_{\odot}$ to H_{noAGN} counterparts. We have checked that relaxing the quite stringent criteria adopted in this work (slightly) improves the matching fraction, but since it also increases the number of false matches and does not alter any of our conclusions, we prefer to restrict ourselves to the more conservative sample defined in this section.

3 DARK MATTER HALO DENSITY PROFILES

Let us first study the evolution of the inner density profiles of dark matter haloes in the three simulations.

3.1 Definitions

Our investigation starts with the evolution of the dark matter component. The questions we want to address here are twofold: 1) Does AGN feedback noticeably modify the inner density profiles of dark matter haloes? and 2) How does the difference between the inner density profiles of H_{AGN} and H_{noAGN} (or H_{DM}) haloes evolve? To do so, we use a systematic object-to-object comparison between the HORIZON-AGN, HORIZON-NOAGN and HORIZON-DM simulations based on the matching procedure described in the previous section. Note that when calculating the density profiles of haloes in the H_{DM} run, we rescale the mass of the DM particles by a factor $(\Omega_{\text{m}} - \Omega_{\text{b}})/\Omega_{\text{m}}$ to make it identical to the mass of DM particles in the baryonic runs.

In the following, we split our H_{AGN} DM halo sample into four different mass intervals: $5 \times 10^{11} (\pm 10\%) M_{\odot}$, $10^{12} (\pm 10\%) M_{\odot}$, $5 \times 10^{12} (\pm 10\%) M_{\odot}$ and $\geq 10^{13} M_{\odot}$, which we match to their H_{noAGN} and H_{DM} counterparts. For each of these four mass bins, we then compute the mean density profiles (binned in spherical shells equally spaced in $\log r$), i.e. $\rho_{\text{AGN}}(r)$, $\rho_{\text{noAGN}}(r)$ and $\rho_{\text{DM}}(r)$ at every redshift. This allows us to consider the evolution of density profiles at fixed halo mass. In addition, we have also considered the evolution of the density profiles of the progenitors of halos within these mass bins at $z = 0$. Thanks to our large simulated volume, each sub-sample consists in general of ten objects or more in the most massive bin and thousands of objects in the least massive one. However, when this is not the case (at high redshift for the most massive objects: see Fig. 1, top panels), we lower the redshift until a minimum of ten haloes of that mass can be identified and an average density profile computed.

In order to study the (relative) evolutions of the mean inner density profiles of dark matter haloes extracted from the three different simulations, we use two estimators. The first one is the *mass-weighted density slope within r_1 and r_2* introduced by Dutton & Treu (2014):

$$\gamma' = \frac{1}{M(r)} \int_{r_1}^{r_2} \gamma(x) 4\pi r^2 \rho(x) dx, \quad (1)$$

where $\gamma \equiv d \log \rho / d \log r$ is the local logarithmic slope of the density profile ρ and M the local mass. Using a discrete representation of the density profiles, we measure $\gamma(r)$ and $M(r)$ for each spherical shell centered on position r . γ' is estimated in the range $[r_1 - r_2] = [1.0 - 5]$ kpc.

Secondly, in order to quantitatively study the evolution of the gap between the different density profiles, we compute the

quantity A_{DM} and A_{noAGN} defined by:

$$A_{\text{DM|noAGN}} = \int_{\log r_1}^{\log r_2} \frac{\rho_{\text{DM|noAGN}}(r) - \rho_{\text{AGN}}(r)}{\rho_{\text{AGN}}(r)} d \log r. \quad (2)$$

A_{DM} and A_{noAGN} give an estimation of the gap between the mean profiles of H_{noAGN} and H_{DM} haloes with respect to the mean profiles of H_{AGN} haloes. In the following, A_{DM} and A_{noAGN} have been estimated in the range $[r_1 - r_2] = [1.0 - 10]$ kpc.

Note that the minimal value adopted for r_1 is dictated by our spatial resolution, which does not allow us to reach smaller scales. Spatial resolution is also the main reason why we decide not to use a fixed fraction of the virial radius to define r_1 (and r_2): we would be restricted to selecting (at least) $r_1 = 0.01 \times r_{\text{vir}}$ at high redshift because haloes are more compact and we cannot probe their inner kpc. In turn, this would then translate into $r_1 \geq 10$ kpc for galaxy cluster size haloes at $z = 0$, which somewhat contradicts our purpose to examine their inner density profile to the best of our ability. For these reasons, we adopt instead a simple fixed physical scale for r_1 and r_2 : we probe the inner 1-5 (γ') or 1-10 ($A_{\text{DM|noAGN}}$) kpc of DM haloes for any redshift and halo mass. The different choice of value for r_2 used for γ' and $A_{\text{DM|noAGN}}$ illustrates the fact that the results presented in this paper are robust to variations of up to a factor 2 in the values of r_1 and r_2 .

3.2 Visual inspection: a three phases scenario?

Fig. 1 shows the averaged spherical density profiles ρ_{AGN} , ρ_{noAGN} and ρ_{DM} derived for haloes pertaining to our different mass sub-samples and at three different redshifts. At a given time, they clearly appear different from one other especially in the central region ($r \lesssim 20$ kpc). Conversely, they seem indistinguishable at large radii, suggesting that the presence of baryons and/or AGN feedback induces noticeable effects only on small scales.

Now, if one analyses the evolution of the mean H_{DM} , H_{noAGN} and H_{AGN} halo density profiles separately, clear trends can be noticed. First, as expected from numerous previous studies, the H_{DM} density profiles are always centrally cuspy: their inner slopes are consistent with a NFW profile (as shown in the next section). Note also that at fixed halo mass, the H_{DM} density profiles are more extended, less concentrated, at present times than at high redshift. This well known result is mainly due to the fact that low redshift haloes have undergone more (major) mergers than their high redshift analogues, and these mergers tend to diffuse material at larger radii (see for instance Klypin et al. 2016). As a consequence, for a fixed mass interval, the density in the halo inner region progressively decreases as more and more mass is distributed at large radii. The H_{noAGN} halo density profiles are always much steeper and have higher central values compared to those in the other simulations. For a fixed mass interval, no significant variation in profile shape as a function of redshift is observed. Finally, the H_{AGN} density profiles present a more complex evolution. At high redshift ($z \geq 4$) the halo density profiles of the two first mass bins (i.e. $5 \times 10^{11} M_{\odot}$ and $10^{12} M_{\odot}$) are quite steep and close to their H_{noAGN} matches. At intermediate redshifts ($z \sim [2.7 - 1.6]$), they appear to have flattened and can even have lower central density values (≤ 5 kpc) than to their H_{DM} counterparts. Finally, at present times, the den-

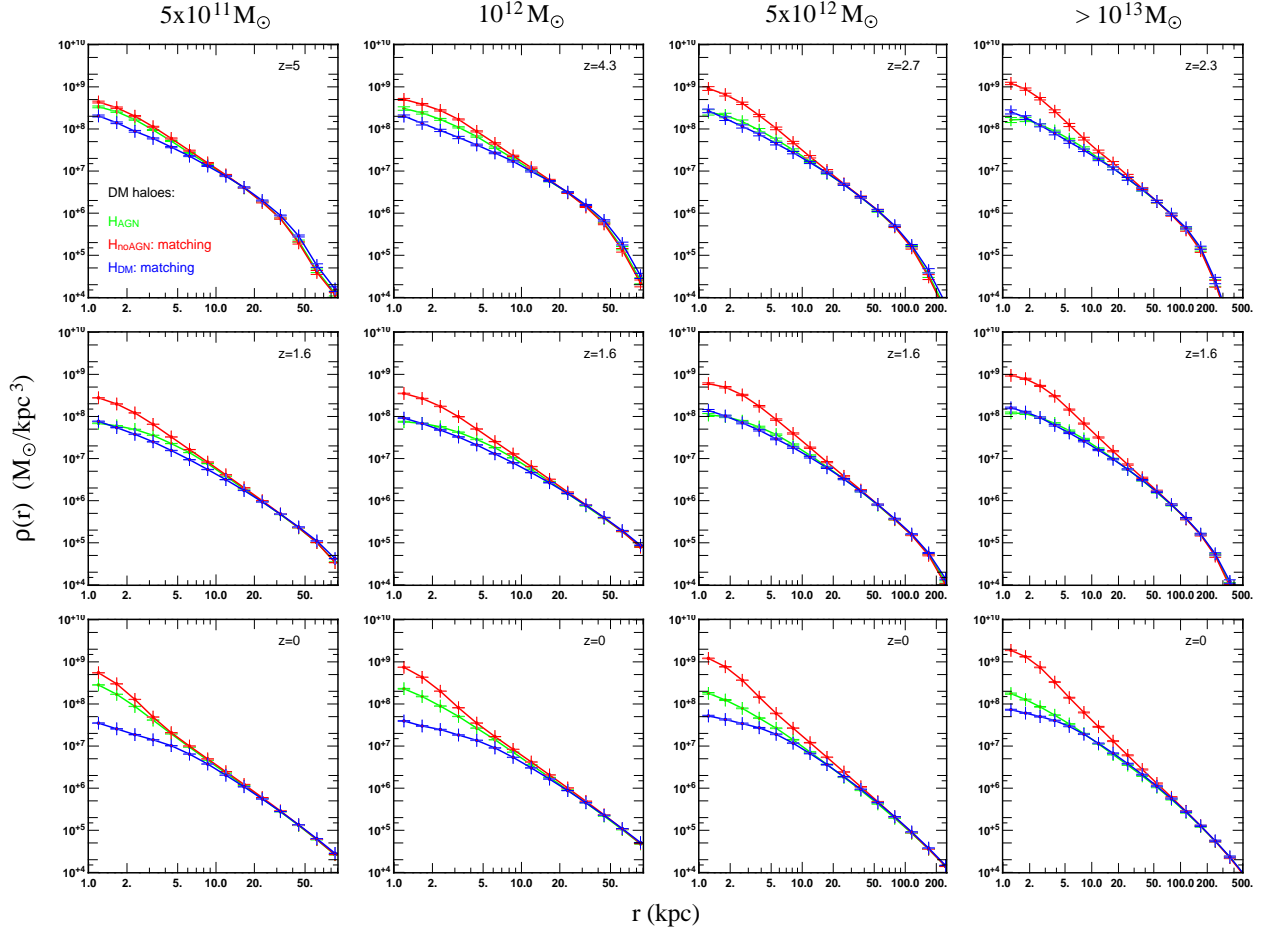


Figure 1. The evolution of the mean density profiles of dark matter haloes extracted from H_{AGN} (green lines), H_{noAGN} (red lines) and H_{DM} (blue lines). We focus on four distinct fixed mass intervals: $\sim 5 \times 10^{11} M_{\odot}$ (first column), $\sim 10^{12} M_{\odot}$ (second column), $\sim 5 \times 10^{12} M_{\odot}$ (third column) and $\geq 10^{13} M_{\odot}$ (fourth column). Three different epochs are also considered: high redshift (first line), intermediate redshift (second line) and $z = 0$ (third line). The error bars correspond to the error on the mean. These plots suggest that H_{noAGN} haloes have always very dense and cuspy central regions. On the contrary, AGN feedback tends to flatten the profiles especially at intermediate redshifts ($z \sim [1.6 - 2.7]$) whereas a “cusp regeneration” is observed at $z = 0$.

sity profiles of H_{AGN} haloes steepen and approach again those of their H_{noAGN} twins. In view of these results, the evolution of H_{AGN} halo density profiles therefore seems to follow three distinct phases.

This scenario is confirmed when studying the evolution of the progenitors of dark matter haloes of mass $5 \times 10^{12} M_{\odot}$ at $z = 0$. The variations of their density profiles are shown at the same three redshifts in Fig. 2. H_{AGN} haloes clearly present a mean density profile that is shallower at $z = 1.6$ than at $z = 5$ or $z = 0$. This strongly suggests the existence of successive phases of expansion and contraction of the mean inner DM halo density profile. Note that at $z = 5$, ρ_{AGN} and ρ_{noAGN} are almost indistinguishable (red and green dotted lines on Fig 2). Since the density profiles of proto-dark matter haloes (i.e. at very high redshifts) of the three simulations are expected to be identical (as galaxy formation has not happened yet), this indicates that H_{AGN} and H_{noAGN} haloes density profiles have undergone a nigh identical first phase of condensation before $z \sim 5$. It is worth mentioning that similar trends are obtained when following the progenitors of the other halo mass subsamples. Finally, as we will see in more detail in section 4, the situation differs for the evolution of galaxy profiles, in the

sense that H_{AGN} stellar density profiles remain quite shallow at low redshift.

3.3 Quantitative trends

The three redshift snapshots presented in Fig. 1 and 2 provide a useful qualitative impression of the general evolution of the mean density profiles of H_{DM} , H_{noAGN} and H_{AGN} haloes. In order to derive more quantitative estimates, we now look at the evolution of the mass-weighted slope of their inner density profile, γ'_{dm} , as defined by equation 1.

Fig. 3 shows the evolution of γ'_{dm} for H_{AGN} DM haloes with a fixed mass of $10^{12} M_{\odot}$ (dotted lines), $5 \times 10^{12} M_{\odot}$ (dashed lines) and $> 10^{13} M_{\odot}$ (solid lines). Results for their H_{noAGN} and H_{DM} counterparts are also presented in the figure. First, as far as H_{DM} haloes are concerned, values of γ'_{dm} are very close to -1 , consistent with NFW profile expectations, although we note that γ'_{dm} is slightly increasing with time by about 0.3. As haloes become more and more extended at low redshift, the range of [1-5] kpc is probing a relatively “deeper” region in terms of fraction of the virial radius compared to that probed for haloes of the same mass at higher

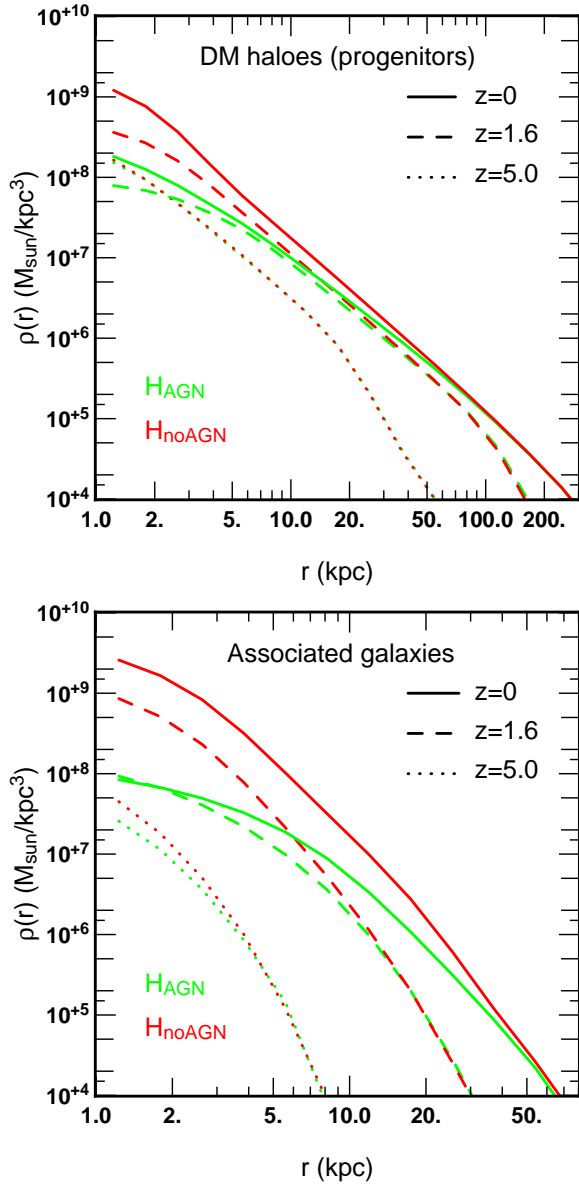


Figure 2. Upper panel: the evolution of the mean density profiles of the progenitors of H_{AGN} dark matter haloes of mass $\sim 5 \times 10^{12} M_{\odot}$ at $z = 0$ (green lines). Three different redshifts have been considered: $z = 5$ (dotted line), $z = 1.6$ (dashed line) and $z = 0$ (solid line). Results for the H_{noAGN} counterpart profiles are shown in red colors. For clarity, we do not show either the H_{DM} counterpart profiles or the error bars (which are similar to those in Fig. 1). As for Fig. 1, the mean density profile of dark matter haloes is flatter at intermediate redshift ($z \sim 1.6$) and steeper at high and low z . The lower panel shows the corresponding situation for the associated galaxies. In this case, when AGN feedback is included, the profiles of galaxies progressively flatten all the way to $z = 0$.

redshifts. Second, as expected from adiabatic contraction considerations (e.g. Blumenthal et al 1986), the inner density profiles of H_{noAGN} are always very steep with slopes that are close to -2 . In this case a slight decrease, of a similar amplitude to the increase noted for H_{AGN} haloes, is observed in the evolution of γ'_{dm} . Finally, H_{AGN} haloes with a fixed mass of $10^{12} M_{\odot}$ clearly exhibit shallower inner density slopes at $z \sim [1.5-1.0]$ than at higher or lower redshift, thus confirm-

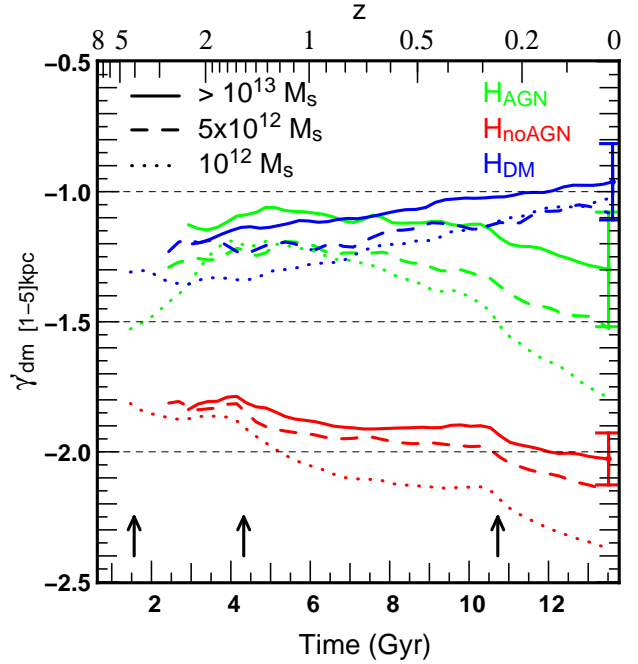


Figure 3. Time evolution of the mean mass-weighted density slope γ'_{dm} (estimated within [1-5] kpc) of DM haloes with masses $10^{12} M_{\odot}$ (dotted lines), $5 \times 10^{12} M_{\odot}$ (dashed lines) and $> 10^{13} M_{\odot}$ (solid lines). Slopes measured for HORIZON-AGNhaloes and matched HORIZON-NOAGN and HORIZON-DM counterparts are coloured in green, red and blue respectively. The three arrows indicate the times when a new refinement level is added in the simulations. For clarity we do not show the corresponding evolution for the $5 \times 10^{11} M_{\odot}$ mass interval as it is similar to those derived for haloes of mass $10^{12} M_{\odot}$. Typical dispersions are indicated by vertical error bars at $z = 0$.

ing the more qualitative results extracted from Fig. 1. Similar trends are observed for lower haloes masses (i.e. $5 \times 10^{11} M_{\odot}$) but not shown in Fig. 3 for sake of clarity. More massive haloes, with masses $5 \times 10^{12} M_{\odot}$ and $> 10^{13} M_{\odot}$, generally take more time to reach their final mass, so that our analysis of their mean density profiles can only start from redshift $z = 2.7$ and $z = 2.3$ respectively (see Fig. 1). Due to the non-negligible past AGN activity they have already experienced by that time, one can notice that H_{AGN} haloes of these mass sub-samples already feature profiles that are quite flat and can even have mean slopes lower than their H_{DM} counterparts. On the contrary, at low redshift ρ_{AGN} profiles steepen considerably, with γ' reaching values well below -1 , and close to -1.5 by $z = 0$, thereby confirming the visual trends highlighted in Fig. 1. It is also worth mentioning that at any given redshift, more massive haloes tend to have flatter inner density profiles than low mass ones, which confirms that AGN feedback impact increases with halo mass. To give explicit numbers, at $z = 0$, density profiles of haloes with masses $> 10^{13} M_{\odot}$, $5 \times 10^{12} M_{\odot}$, $10^{12} M_{\odot}$ and $5 \times 10^{11} M_{\odot}$ boast an inner slope value of ~ -1.3 , ~ -1.5 , ~ -1.8 and -2.1 respectively (the latter is not shown in Fig. 3).

Fig. 4 shows the evolution of γ'_{dm} for the progenitors of dark matter haloes that have a mass of $5 \times 10^{12} M_{\odot}$ either at $z = 1.0$ or $z = 0.0$. Focussing first on the highest redshifts ($z > 2$), H_{AGN} and H_{noAGN} profiles are clearly much steeper than H_{DM} ones. As previously mentioned, this is mainly due to the galaxy formation process: radiative cooling and subse-

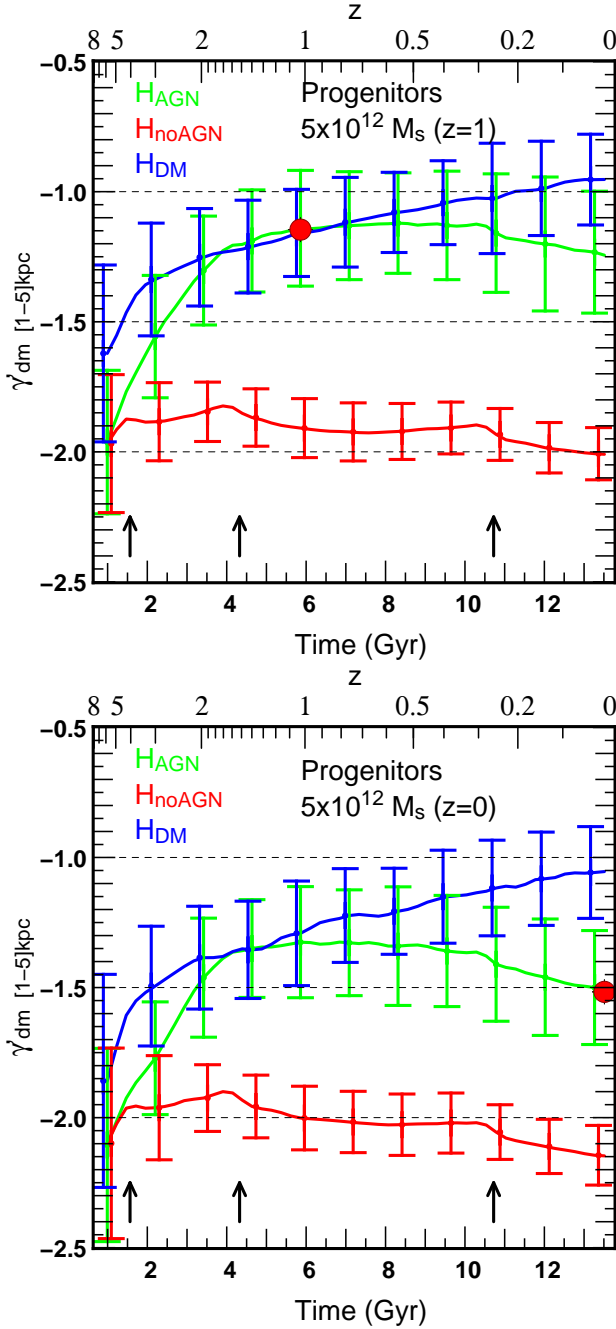


Figure 4. Time evolution of the mass-weighted density slope γ'_{dm} of progenitors of DM haloes with a mass of $5 \times 10^{12} M_{\odot}$ at $z = 1$ (upper panel) and $z = 0.0$ (lower panel). The mean slope has been estimated in the range of [1-5]kpc. Results from HORIZON-AGN, HORIZON-NOAGN and HORIZON-DM simulations are coloured in green, red and blue respectively. The three arrows indicate the times when a new refinement level is added in the simulations. The error bars correspond to the standard deviation. To facilitate comparison, filled red circles in each panel indicate the values of γ'_{dm} when H_{AGN} dark matter haloes reach a mass of $5 \times 10^{12} M_{\odot}$. In spite of belonging to the same mass sub-sample, H_{AGN} haloes at $z = 0.0$ tend to have steeper profiles than those at $z = 1$.

quent star formation lead to a steepening of the DM density profile of DM haloes due to adiabatic contraction (Blumenthal et al. 1986; Gnedin et al. 2004), in agreement with previous works (e.g., Gustafsson et al. 2006; Romano-Díaz et al. 2008; Abadi et al. 2010; Pedrosa et al. 2010; Tissera et al. 2010; Duffy et al. 2010). Note that the mean slopes of H_{AGN} and H_{noAGN} halo density profiles are very close at $z \sim 5$ suggesting that AGN feedback has not had an important impact yet by this redshift. Fast forwarding to $z \sim 1.6$, whilst the mean profile of H_{noAGN} haloes remains very steep with a slope close to -2 , that of their H_{AGN} counterparts is progressively flattened by AGN feedback, in good agreement with the results reported in Peirani et al. (2008) and Martizzi et al. (2013). Finally, from $z \sim 1.6$ to present times, ρ_{AGN} becomes slightly steeper as the mean inner slope of H_{AGN} haloes progressively decreases by 0.1. The two panels of Fig. 4 explain the origin of the difference in the slope of H_{AGN} halo density profiles at fixed halo mass for intermediate and low redshifts displayed in Fig. 3: H_{AGN} haloes tend to have steeper inner profiles at low redshift because they have undergone a phase of “cusp regeneration”. For completeness sake, we recall that additional refinement levels are triggered at $z \sim 5$, $z \sim 1.5$ and $z \sim 0.26$. They induce a sudden increase in star formation and black hole accretion at these different epochs as the gas is allowed to collapse to higher densities. These abrupt changes slightly affect the evolution of γ'_{dm} especially in the case H_{noAGN} haloes, as shown on Fig. 4.

Hence the evolution of the inner part of ρ_{AGN} does exhibit three successive phases which are quantitatively differentiable. A first condensation phase, from very high redshifts to $z \sim 5$ where dissipative galaxy formation processes and consequent adiabatic contraction of dark matter haloes dominate. This stage is then followed by a flattening phase, driven by important AGN activity until $z \sim 1.6$. Finally, a second condensation phase or cusp regeneration occurs from $z \sim 1.6$ down to $z = 0$ as AGN activity slowly subsides. To understand this latter phase, one can study the evolution of AGN activity in the relevant dark matter halo sub-samples. Indeed, an analysis of the evolution of gas mass accretion onto black holes (BHs) $\dot{M}_{\text{BH}} \equiv dM_{\text{BH}}/dt$ for progenitors of DM haloes taken from each mass sub-sample and displayed in Fig. 5 reveals that for any given halo mass sample, \dot{M}_{BH} and therefore AGN activity progressively decrease with time. In spite of the noticeable bumps induced by the addition of new refinement levels which artificially boost accretion, \dot{M}_{BH} is one order of magnitude lower at $z = 0$ than at $z \sim 1.4$. The cusp regeneration phase measured in the evolution of γ'_{dm} is most probably related to the fading of AGN activity at lower redshifts. As emphasised by Peirani et al. (2008) and Martizzi et al. (2013), the flattening of dark matter halo inner density profiles is due to a repetitive cycle of rapid gas expansions driven by AGN feedback and slower contractions as gas cools and falls back, which increases the velocity dispersion of the dark matter particles. If AGN activity progressively dwindles, this mechanism becomes less efficient at counterbalancing DM adiabatic contraction and thus keeping the DM density profiles flat. Fig. 5 also shows the evolution of the Eddington ratio $\chi \equiv \dot{M}_{\text{BH}}/\dot{M}_{\text{Edd}}$ (where \dot{M}_{Edd} is the Eddington accretion rate) for the same haloes. These results suggest that the radio mode tends to be the dominant mode below $z \lesssim 2$. A similar behaviour is observed when considering haloes of fixed mass, rather than progenitors. Such a redshift dependence of the dominant mode

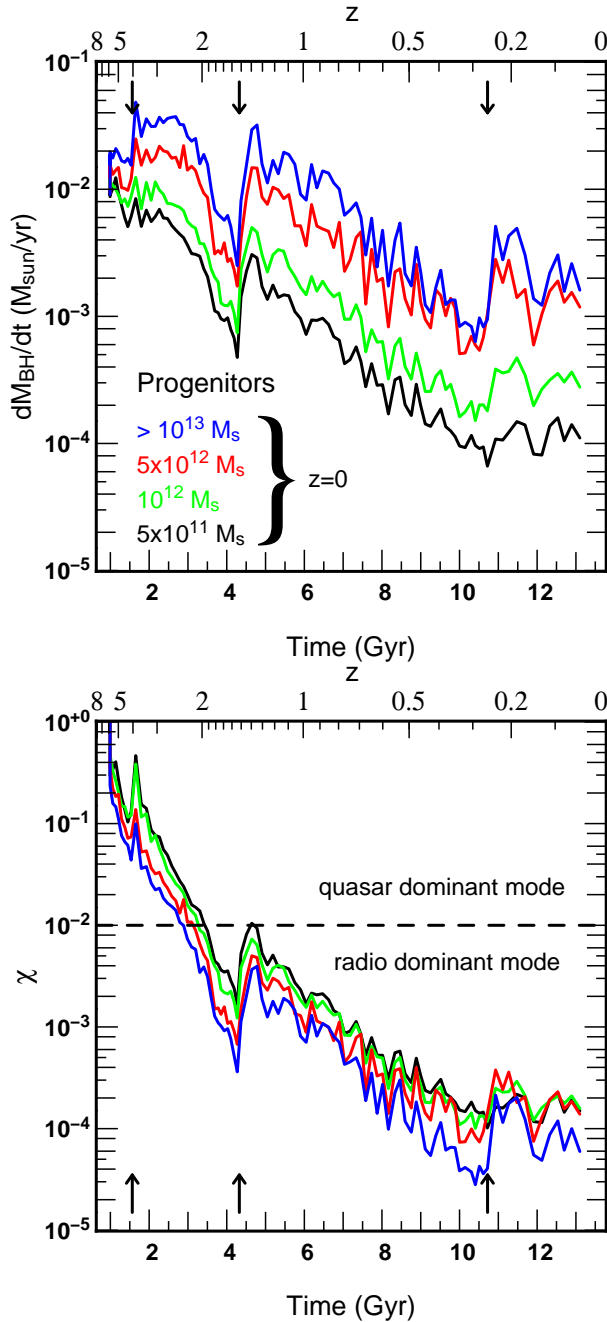


Figure 5. Upper panel: evolution of the median mass accretion onto black holes $M_{\text{BH}} \equiv dM_{\text{BH}}/dt$ for progenitors of DM haloes of mass $5 \times 10^{11} M_{\odot}$ (black line), $10^{12} M_{\odot}$ (green line), $5 \times 10^{12} M_{\odot}$ (red line) and $\geq 10^{13} M_{\odot}$ (blue line) at $z = 0$. Lower panel: median Eddington ratio $\chi \equiv M_{\text{BH}}/M_{\text{Edd}}$ where M_{Edd} is the Eddington accretion rate. Arrows indicate when an additional level of refinement is added in the simulation. For a given halo mass, the mass accretion onto black holes and therefore the AGN activity is much lower at low redshifts where the radio mode dominates.

is also in agreement with Volonteri et al. (2016) who have studied in detail the cosmic evolution of black holes in the HORIZON-AGN simulation. These authors found that the evolution of the luminosity function (LF) in HORIZON-AGN is consistent with the existing observational determination of the bolometric LF (Hopkins et al. 2007; Shankar et al. 2009; Ueda

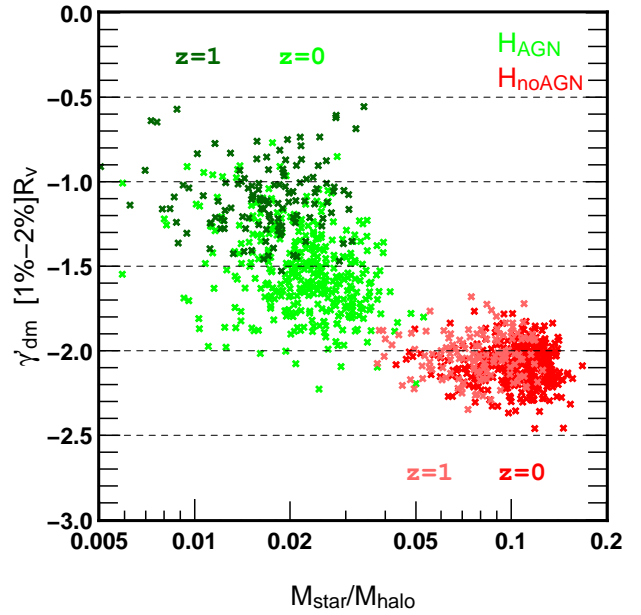


Figure 6. Variation of the mass-weighted density slope γ'_{dm} of DM profiles within [1-2]% of the virial radius as a function of the ratio $M_{\text{star}}/M_{\text{halo}}$ for H_{AGN} haloes of mass $\geq 10^{13} M_{\odot}$ (green crosses) and matching H_{noAGN} haloes (red crosses) identified at $z = 1$ (light colors) and $z = 0$ (dark colors). Dark matter haloes with a higher $M_{\text{star}}/M_{\text{halo}}$ ratio tend to have steeper inner profiles.

et al. 2014) provided there exists a transition at $z \sim 2$ between quasar and radio dominated mode (see their Fig. 13). Recall that in the HORIZON-AGN simulation, the explosive quasar mode consists in an isotropic injection of thermal energy into the surrounding gas while at low accretion rates, the more quiescent radio mode deposits AGN feedback energy into a bipolar outflow (see Dubois et al. 2010 for a complete description). It is therefore not very surprising that such a transition also affects the evolution of inner dark matter halo profiles, since the radio mode of AGN feedback mainly prevents hot gas from cooling and eject little gas from the galaxy (Beckmann et al. in prep).

The cusp regeneration phase was already observed by Di Cintio et al. (2014) and Tollet et al. (2016) in hydrodynamical simulations focusing on lower mass haloes (i.e. $M_{\text{halo}} < 10^{12} M_{\odot}$). These authors claimed that the density slope of DM haloes mainly depends on the ratio between stellar mass and total halo mass $M_{\text{star}}/M_{\text{halo}}$, with large ratios ($M_{\text{star}}/M_{\text{halo}} > 0.01$) corresponding to contracted profiles. Fig. 6 shows the variation of the slope of DM halo density profiles, estimated this time within 1-2 % of the virial radius, as a function of the ratio $M_{\text{star}}/M_{\text{halo}}$ for H_{AGN} haloes of mass $\geq 10^{13} M_{\odot}$ and matching H_{noAGN} haloes. We find that in general, our haloes have values of $M_{\text{star}}/M_{\text{halo}}$ greater than 0.01 and slopes steeper than -1, indicative of contraction. At $z = 0$, H_{AGN} haloes have steeper density profiles and higher $M_{\text{star}}/M_{\text{halo}}$ values compared to haloes of the same mass at $z = 1$. Moreover, in the absence of AGN feedback, higher values of $M_{\text{star}}/M_{\text{halo}} \gtrsim 0.05$ are obtained which are associated to steeper profiles ($\gamma'_{\text{dm}} \sim -2$). This suggests that γ'_{dm} is strongly correlated with $M_{\text{star}}/M_{\text{halo}}$, thus corroborating the previous findings of Di Cintio et al. (2014) and Tollet et al. (2016). However, it is worth mentioning that their simulations

did not include AGN feedback and therefore are difficult to extrapolate to high mass haloes. Nonetheless, we remark that our results from H_{noAGN} haloes are in fair agreement with the predictions of their fitting function for $M_{\text{star}}/M_{\text{halo}} > 0.05$.

3.4 Evolution of the gap between ρ_{AGN} , ρ_{noAGN} and ρ_{DM}

In this section, we study the evolution of A_{DM} and A_{noAGN} defined by equation 2 which monitors how the relative gaps between ρ_{AGN} , ρ_{noAGN} and ρ_{DM} evolve. The variations of A_{DM} and A_{noAGN} are thus expected to provide complementary information to the evolution of the slope of dark matter halo density profiles previously studied.

3.4.1 H_{AGN} vs H_{DM}

Let us start with the relative evolution of ρ_{DM} and ρ_{AGN} . Fig. 7 shows the variations of A_{DM} for the haloes of our four considered mass intervals at $z = 0$ (top panel) and their progenitors (bottom panel). Three successive phases can clearly be identified again, particularly when looking at the bottom panel of Fig. 7. At very high redshift, A_{DM} tends to 0 as galaxy formation has yet to significantly affect the inner structure of dark matter haloes. Then, from very high redshift to $z \sim 3$, A_{DM} becomes progressively more and more negative due to rapid galaxy formation and subsequent dark matter adiabatic contraction. From $z \sim 3$ to $z \sim [1.6 - 1.2]$, A_{DM} is increasing whilst retaining its negative value. This suggests again that AGN activity is reducing the central density (and the inner density slope) of H_{AGN} haloes which results in reducing the gap w.r.t. the matching H_{DM} haloes density profiles. Finally, from $z \sim [1.6 - 1.2]$ to $z = 0$, A_{DM} decreases again, always remaining negative. The gap between the inner density profiles of H_{AGN} and H_{DM} haloes thus progressively becomes more and more important since this time the central density (and the inner density slope) of H_{AGN} haloes is increasing (phase of cusp regeneration). Note that the second phase (i.e. flattening of H_{AGN} DM halo density profiles) occurs sooner and lasts longer for more massive objects. Furthermore, the third phase occurs later for more massive objects. This reinforces our conclusions based on the evolution of inner profile density slopes that AGN feedback impacts more durably and significantly the most massive haloes.

A similar conclusion can be drawn when studying the time evolution of A_{DM} for haloes with a fixed mass, independent of cosmic time, as displayed in the top panel of Fig. 7. A_{DM} is increasing at high redshifts ($5 > z > 2$) for the first three lower mass intervals while keeping negative values. These black, green and red curves reach a maximal value at redshifts around 1.6, 1.6 and 1.2 respectively: AGN activity has efficiently reduced the central density as well as flattened the profiles of H_{AGN} haloes, leading to the reduction of the gap between inner density profiles of H_{AGN} and matching H_{DM} haloes. Note that for these three mass intervals, A_{DM} is already negative at high redshift due to DM adiabatic contraction induced by galaxy formation having already taken place in such massive haloes. Then, after each peak, A_{DM} monotonically decreases until $z = 0$ (phase of cusp regeneration). For the most massive haloes ($\geq 10^{13} M_{\odot}$), A_{DM} is mainly decreasing but remains positive until $z \sim 1$ indicating that H_{AGN}

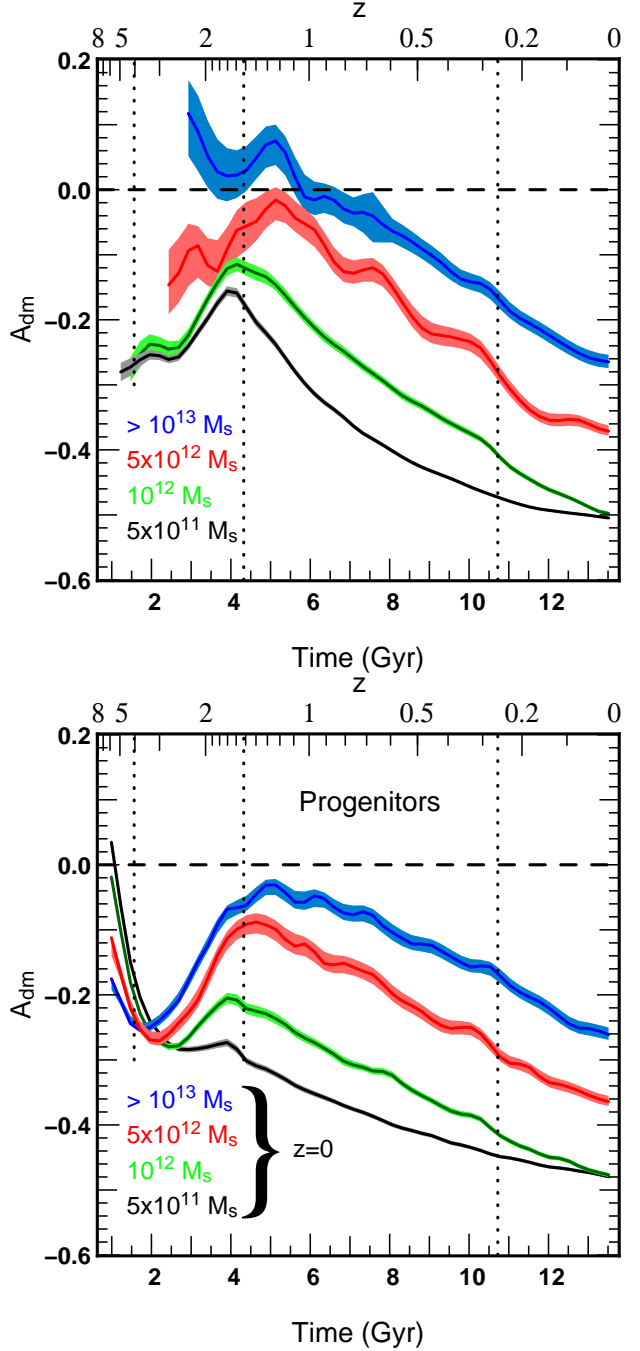


Figure 7. Time evolution of A_{DM} which measures the gap between H_{AGN} and matched H_{DM} dark matter halo density profiles in the range of [1-10] kpc. The upper panel considers haloes within fixed mass intervals, independently of cosmic time while the lower one follows the evolution of A_{DM} for the progenitors of haloes of mass $\sim 5 \times 10^{11}$, $\sim 10^{12}$, $\sim 5 \times 10^{12}$ and $\geq 10^{13} M_{\odot}$ at $z = 0$. The vertical dashed lines indicate when additional levels of refinement are triggered. The shaded areas represent the error on the mean.

haloes of this mass at higher redshifts have lower central density (and also flatter density profiles) than their H_{DM} counterparts. This also reinforces that AGN activity has a stronger impact on the inner DM density profiles of the most massive haloes.

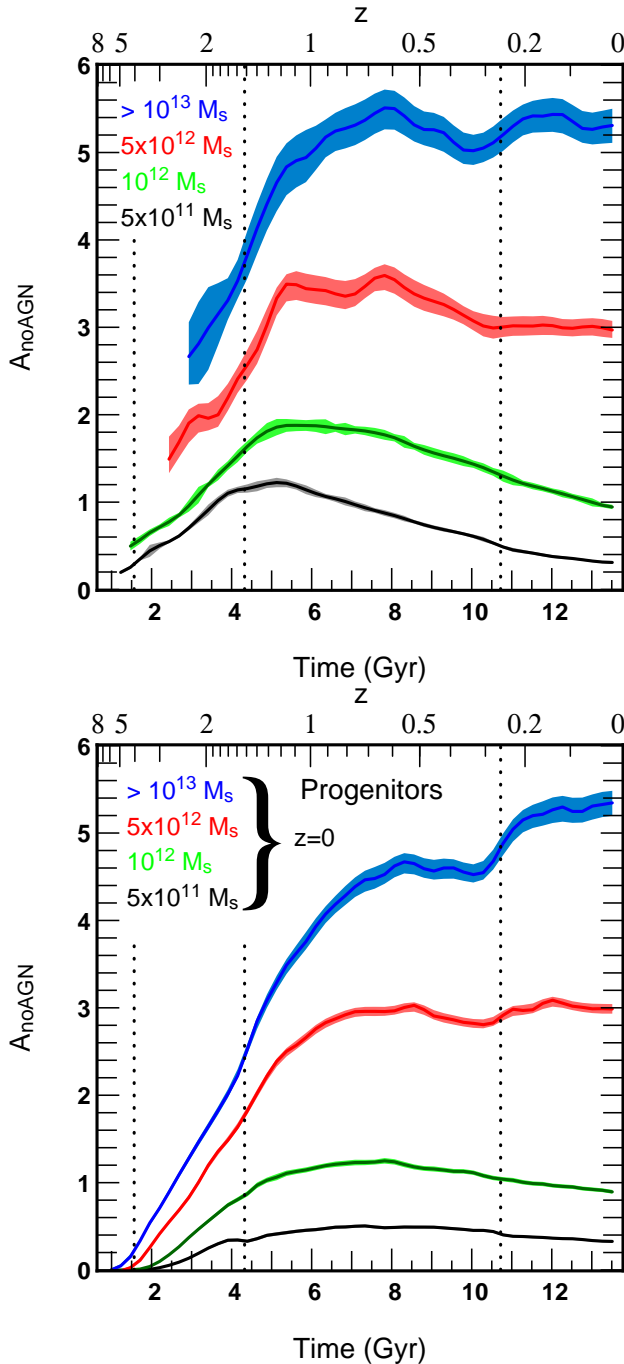


Figure 8. Time evolution of A_{noAGN} , which measures the gap between H_{AGN} and matching H_{noAGN} DM halo density profiles in the range of [1–10] kpc. Upper and lower panels consider haloes within fixed mass intervals across cosmic time and the progenitors of haloes with masses of $\sim 5 \times 10^{11}$, $\sim 10^{12}$, $\sim 5 \times 10^{12}$ and $\geq 10^{13} M_{\odot}$ at $z = 0$ respectively. The vertical dashed lines indicate when additional levels of refinement are triggered in the simulation. Shaded areas represent the error on the mean.

3.4.2 H_{AGN} vs H_{noAGN}

AGN feedback manifests itself through two effects. First, it reduces star formation rates in massive galaxies and therefore the amount of stellar material present in their central parts. Second, as we have previously discussed, it flattens the DM host halo density profile, especially at intermediate redshifts. As a result, the central dark matter profiles of H_{AGN} haloes should always be less steep and have lower central values when compared with their H_{noAGN} halo counterparts. In other words, A_{noAGN} must always be positive.

Fig. 8 shows the variation of A_{noAGN} for both progenitors and haloes within fixed mass intervals and confirms again the trends previously pointed out. In the top panel, for the three less massive halo mass intervals, the gap between the DM halo density profiles in H_{AGN} and H_{noAGN} first increases until it reaches a maximum value for z close to 1.2. It then slightly decreases as the redshift progresses towards $z = 0$. For the most massive haloes, with masses $\geq 10^{13} M_{\odot}$, the gap is essentially always increasing until $z = 0.8$ after which it remains constant until $z = 0$. This is consistent with our previous result: the effect of AGN feedback (quasar mode) is more efficient at high redshift, leading to a rapid increase of the gap between the H_{AGN} and H_{noAGN} DM halo profiles. Then, in a longer and later phase between $1.2 \geq z \geq 0$, AGN activity diminishes, and the gap narrows slightly.

The bottom panel of Fig. 8 presents the variations of A_{noAGN} focusing on the evolution of the DM halo profiles of the progenitors of haloes with a mass of $5 \times 10^{11} M_{\odot}$, $10^{12} M_{\odot}$, $5 \times 10^{12} M_{\odot}$ and $\geq 10^{13} M_{\odot}$ at $z = 0$. Here again, at very high redshift, A_{noAGN} is close to 0 for all considered mass intervals since AGN feedback has not yet kicked in. The gap between H_{AGN} and H_{noAGN} haloes then increases until $z \sim [1 - 0.6]$ and stays roughly constant afterwards. It is worth mentioning again that adding an extra refinement level at $z \sim 1.5$ and $z \sim 0.25$ causes spurious artefacts to appear in the otherwise rather smooth evolution of A_{noAGN} . This corresponds to a sudden better force resolution and enhanced gas condensation which has a more dramatic effect in HORIZON-NOAGN than in HORIZON-AGN, where it is somewhat compensated by a simultaneous rise in AGN activity.

4 STELLAR DENSITY PROFILES

4.1 General trends

In the following, we compare the stellar density profiles of galaxies in the same way as we previously did for the dark matter component: we use a systematic (AGN) galaxy to (noAGN) galaxy object-to-object comparison using our matching procedure. We also focus our analysis on four (H_{AGN}) galaxy stellar mass intervals: $10^9 (\pm 10\%) M_{\odot}$, $10^{10} (\pm 10\%) M_{\odot}$, $10^{11} (\pm 10\%) M_{\odot}$ and $\geq 5 \times 10^{11} M_{\odot}$.

Fig. 9 displays spherically averaged galaxy stellar mass density profiles, $\rho_{*,\text{AGN}}$ and matching $\rho_{*,\text{noAGN}}$, derived for each of the four stellar mass bins and at three different redshifts. For the lowest mass interval (i.e. $10^9 M_{\odot}$), we notice no significant difference between H_{AGN} and H_{noAGN} galaxy density profiles: this is not very surprising as AGN feedback is not thought to be effective in such low mass objects. For the three most massive mass intervals, clear gaps between $\rho_{*,\text{AGN}}$ and $\rho_{*,\text{noAGN}}$ can be seen in the central regions, and up to

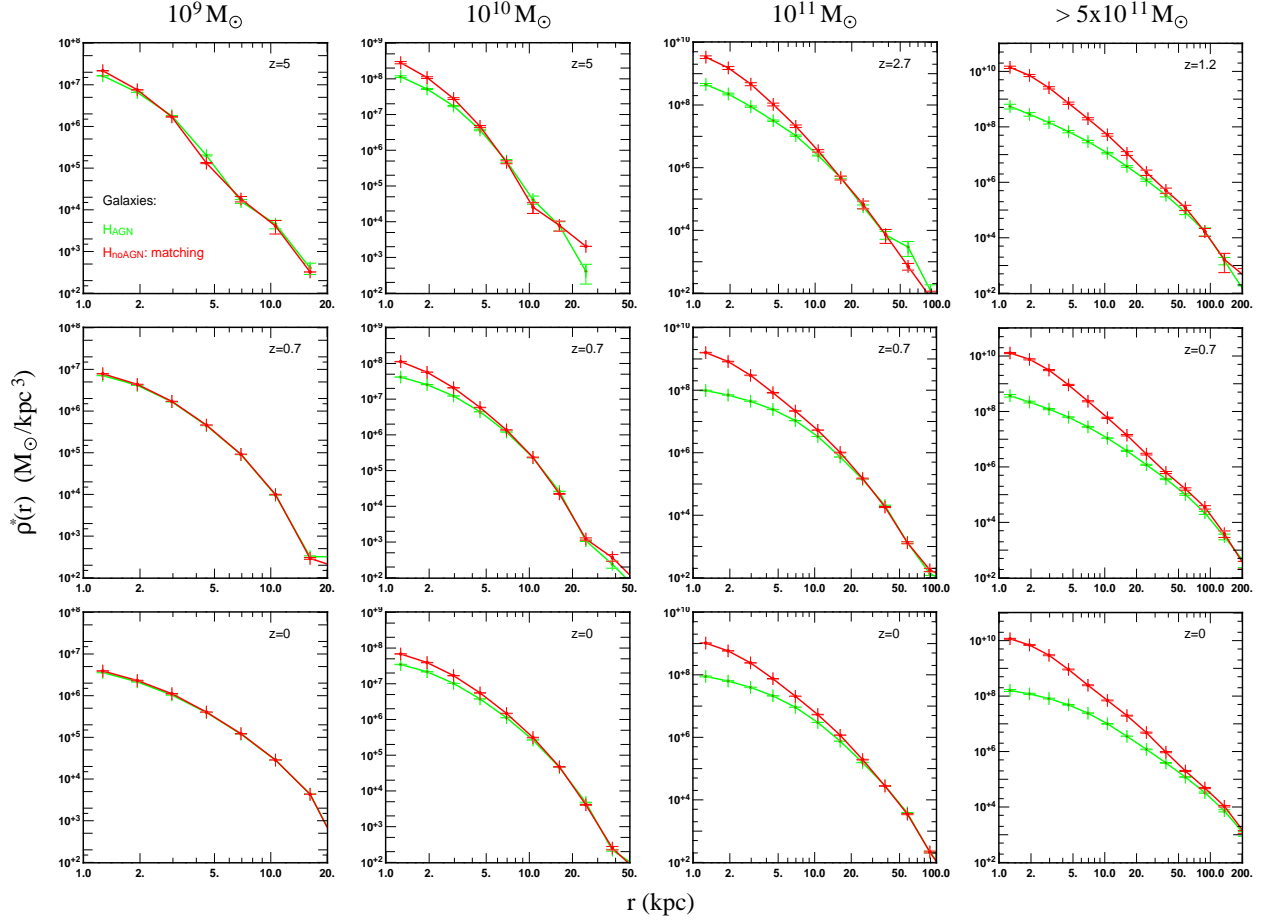


Figure 9. Evolution of the mean stellar density profiles of galaxies extracted from H_{AGN} (green lines) and H_{noAGN} (matching, red lines). We divide our galaxy sample on four fixed mass intervals: $\sim 10^9 M_{\odot}$ (first column), $\sim 10^{10} M_{\odot}$ (second column), $\sim 10^{11} M_{\odot}$ (third column) and $\geq 5 \times 10^{11} M_{\odot}$ (fourth column). As for the DM haloes, three different epochs are considered: high redshift (first row), $z = 0.7$ (second row) and $z = 0$ (third row). The error bars correspond to the error on the mean. The discrepancy between density profiles is all the more important than galaxies are massive. Moreover, the mean H_{AGN} stellar density profiles remain quite flat at low redshift.

a radius of 50 kpc for the most massive galaxies. Moreover, the gap between inner density profiles is all the more important than the galaxies are massive, and increases slightly with time. Similarly to what we observe for the dark matter component, stellar density profiles with and without AGN feedback are similar at large radii. However, in contrast to what happens for dark matter haloes, H_{AGN} galaxy density profiles remain quite flat at low redshift, as already suggested by Fig. 2. Such a behaviour is also more consistent with observations (e.g. Kormendy et al. 2009).

Note that, at a given mass, galaxies are in general more extended at low redshifts because they experience more mergers that tend to spread material at large radii, which increase their effective radius over time (Khochfar & Silk 2006; Bournaud, Jog & Combes 2007; Naab, Johansson & Ostriker 2009; Peirani et al 2010; Oser et al. 2010, 2012; Shankar et al. 2013; Welker et al. 2015; Rodriguez-Gomez et al. 2016). This effect is more pronounced with AGN feedback since the in situ star formation is regulated by AGN activity, at the benefit of the accreted stellar mass in the overall stellar mass budget (Dubois et al. 2013, 2016).

In order to derive a more quantitative evolution, we first study the evolution of the galaxy mass-weighted density slope

γ'_* measured within [1-5] kpc for H_{AGN} galaxies within a fixed mass bin, independent of cosmic time, and their matching H_{noAGN} counterparts. This evolution is displayed in Fig. 10. For galaxies with masses of $10^{10} M_{\odot}$, $10^{11} M_{\odot}$ and $> 5 \times 10^{11} M_{\odot}$ H_{AGN} , we see clear differences when AGN is included or not. Stellar density profiles of H_{AGN} galaxies always display shallower inner slopes than their H_{noAGN} counterparts. Therefore, as was measured for the DM component, AGN feedback tends to flatten the inner stellar density profiles of massive galaxies. We also note that H_{AGN} mean stellar density slopes increase rapidly at high redshift ($z > 1.5$) and then stall at lower z , as a consequence of the evolution of black holes growth and AGN activity history reported in Fig. 5. Finally, the most massive H_{AGN} galaxies tend to have a flatter inner profiles at any given redshift than their lower mass equivalents, which suggest again that AGN feedback plays a more important role in shaping more massive objects.

We derived in Fig. 11 the evolution of γ'_* (estimated within [1-5] kpc) for the progenitors of galaxies of mass $10^{11} M_{\odot}$ at $z = 0$. At high redshift ($z > 5$), since AGN activity has not yet picked up, the density slopes of H_{AGN} and H_{noAGN} galaxies are very similar. Then, from $z \sim 5$ to $z \sim 1$, AGN feedback strongly flattens the density profiles of H_{AGN}

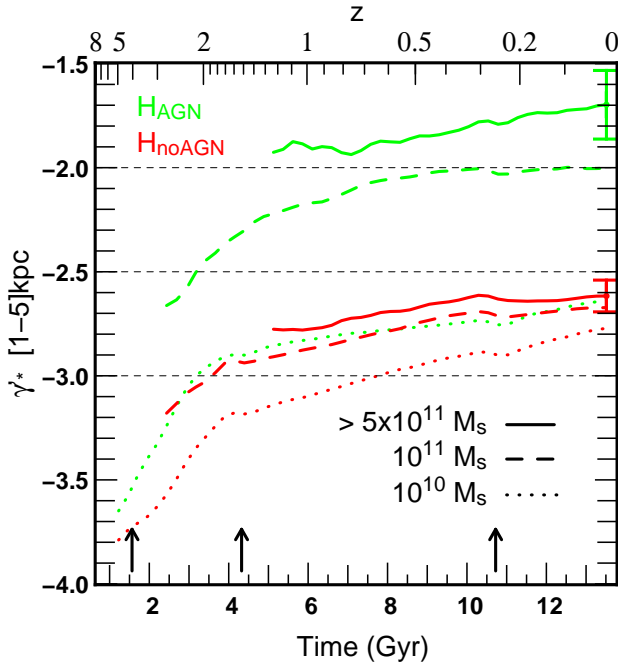


Figure 10. Evolution of the galaxy mass-weighted density slope γ_*^* estimated within [1-5]kpc. We show results for the three more massive H_{AGN} galaxy mass intervals (green colour) and matched H_{noAGN} galaxies (red colour). The three arrows indicate the times when an additional refinement level is added to the simulations. Typical standard deviations are represented by vertical error bars at $z = 0$. AGN feedback significantly and monotonically flattens the inner stellar density profiles of galaxies.

galaxies. At lower redshifts, the inner stellar density profile slopes remain almost constant or increase slightly which confirms trends seen in Fig. 2. It is worth mentioning that similar results are also obtained for progenitors of galaxies with a mass of $\geq 5 \times 10^{11} M_{\odot}$ at $z = 0$.

Finally, Fig. 12 shows the time evolution of A_{noAGN}^* for galaxies within a mass interval fixed throughout cosmic time (right panels). We use the same definition of A_{noAGN} (but for galaxies) given by equation 2 and consider this time $r_1 = 1$ kpc and $r_2 = 5$ kpc. As expected, for $10^9 M_{\odot}$ galaxies, A_{noAGN} stays constant and equal to 0. On the contrary, for $10^{10} M_{\odot}$ galaxies, A_{noAGN}^* is always positive and slightly decreasing below $z \sim 2$. Although AGN activity is relatively weak in galaxies pertaining to this mass range, it still affects their stellar density profiles all the way to the present time. More massive galaxies, with masses of $10^{11} M_{\odot}$ feature a rapid increase in A_{noAGN}^* until $z \sim 1$ and this quantity then remains roughly constant between $z = 1$ and $z = 0$. Finally, A_{noAGN}^* is monotonously increasing for the most massive galaxies ($\geq 5 \times 10^{11} M_{\odot}$). This is explained by two main reasons. First, AGN activity rapidly flattens H_{AGN} galaxy density profiles at high redshift, and second, the mass of H_{noAGN} galaxies is still noticeably increasing down to $z = 0$, as there is no upper limit in this mass range. Fig. 12 also presents the evolution of the progenitors of these galaxies (left panels). In this case, A_{noAGN}^* is always increasing (albeit more rapidly for more massive galaxies) which means that the gap between H_{AGN} and H_{noAGN} galaxy density profiles is continuously increasing. Note again that the additional refinement levels have

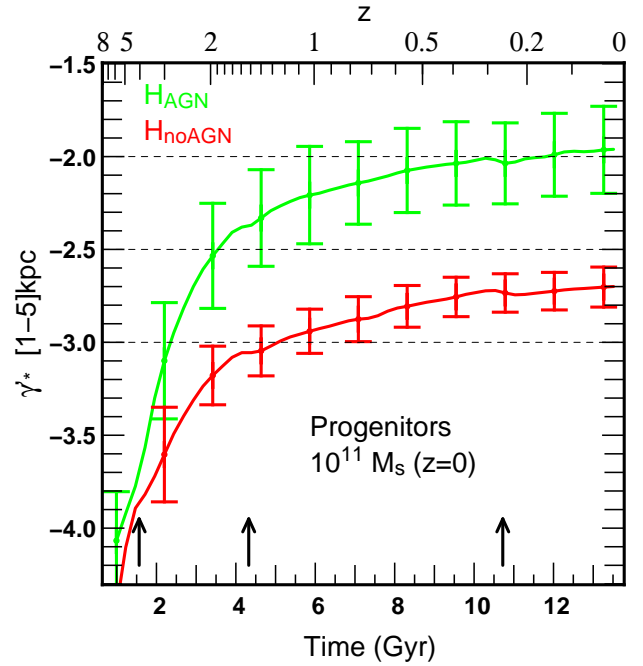


Figure 11. Time evolution of the mass-weighted density slope γ_*^* of the progenitors of galaxies with masses $10^{11} M_{\odot}$ at $z = 0$. Results from H_{AGN} galaxies and their matching H_{noAGN} counterparts are displayed in green and red colours respectively. The three arrows represent epochs where an additional refinement level is added in the simulations. Error bars indicate the standard deviation. H_{AGN} galaxy stellar density profiles are rapidly flattened until $z \sim 1$. Without AGN feedback, galaxy density profiles always remain relatively steep.

a limited but noticeable impact on the evolution of A_{noAGN}^* . The extra star formation spuriously induced at these epochs increases the central stellar mass, especially in H_{noAGN} galaxies, which causes the more pronounced increases seen in the evolution of A_{noAGN}^* . However these numerical effects do not affect our conclusions.

4.2 Matching or no matching, what is the difference?

All along the paper so far, we have only carried out object-to-object comparisons to ensure that we study the properties and evolution of the same objects in the different simulations. However, one can also be interested in comparing the evolution of the properties of objects of similar mass between the three simulations, which is not enforced by the matching strategy. In this section we examine what the difference is between these two approaches.

As far as the dark matter component is concerned, the answer is none, because AGN feedback does not significantly affect the virial mass of DM haloes. This is demonstrated in Fig. 13 where we plot the mean density profiles of H_{noAGN} dark matter haloes either at $z = 1$ or $z = 0$, either obtained through matching or simply considering the population in the same mass interval: the two are indistinguishable from one another.

On the contrary, stellar density profiles of galaxies prove to be very different. Indeed, for any given stellar mass interval of H_{AGN} galaxies, the H_{noAGN} counterparts are in general much more massive. These galaxies display stellar density val-

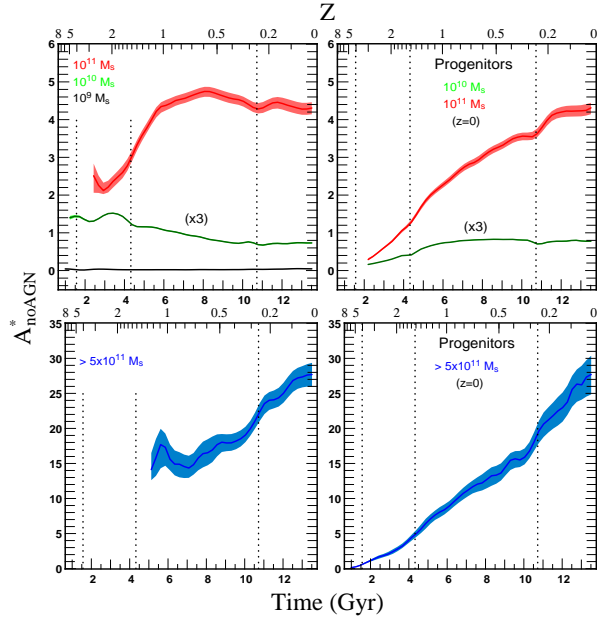


Figure 12. Time evolution of A_{noAGN}^* which measures the gap between H_{AGN} and H_{noAGN} galaxy density profiles in the range of [1-5] kpc. The left panels consider galaxies within fixed mass intervals throughout cosmic time: 10^9 , 10^{10} and $10^{11} M_{\odot}$ (upper panel) and $\geq 5 \times 10^{11} M_{\odot}$ (lower panel). In the right panels, we follow the evolution of the progenitors of galaxies that have a (H_{AGN}) mass of $\sim 10^{10}$, 10^{11} and $\geq 5 \times 10^{11} M_{\odot}$ at $z = 0$. Shaded areas represent the error on the mean. Vertical dashed lines indicate when an additional level of refinement is introduced in the simulations. Note that we have multiplied results obtained for $10^{10} M_{\odot}$ galaxies by a factor 3 for clarity.

ues that are much higher in the central parts but similar at large radii to the H_{AGN} ones. Therefore, when comparing H_{AGN} and H_{noAGN} galaxies of the same mass, Fig. 14 clearly shows that these latter still present higher central stellar density values. However, in order to compensate for the extra mass enclosed within these regions, they also exhibit lower densities at large radii. Thus, for a galaxy of a given mass, AGN feedback leads to density profiles that are more centrally flat but also more extended.

5 DISCUSSION AND CONCLUSIONS

By comparing results from two state-of-the-art hydrodynamical cosmological simulations whose only difference is the presence/absence of AGN feedback, and one cosmological simulation without baryons which otherwise shares the same initial conditions, we have explored the impact of AGN feedback on the evolution of the inner density profiles of massive dark matter haloes and galaxies. We focused on dark matter haloes and galaxies with a mass greater than $5 \times 10^{11} M_{\odot}$ and $10^9 M_{\odot}$ respectively. Since the resolution limit of the simulations is 1 kpc (physical), we have only investigated the (relative) variations of halo and galaxy density profiles within a few kpc from their center (i.e. [1-5]kpc or [1-10]kpc). Our findings can be summarized as follows:

- When AGN feedback is included, the mean inner density profiles ρ_{AGN} of massive dark matter haloes undergo successive phases of contraction (steepening) and expansion (flat-

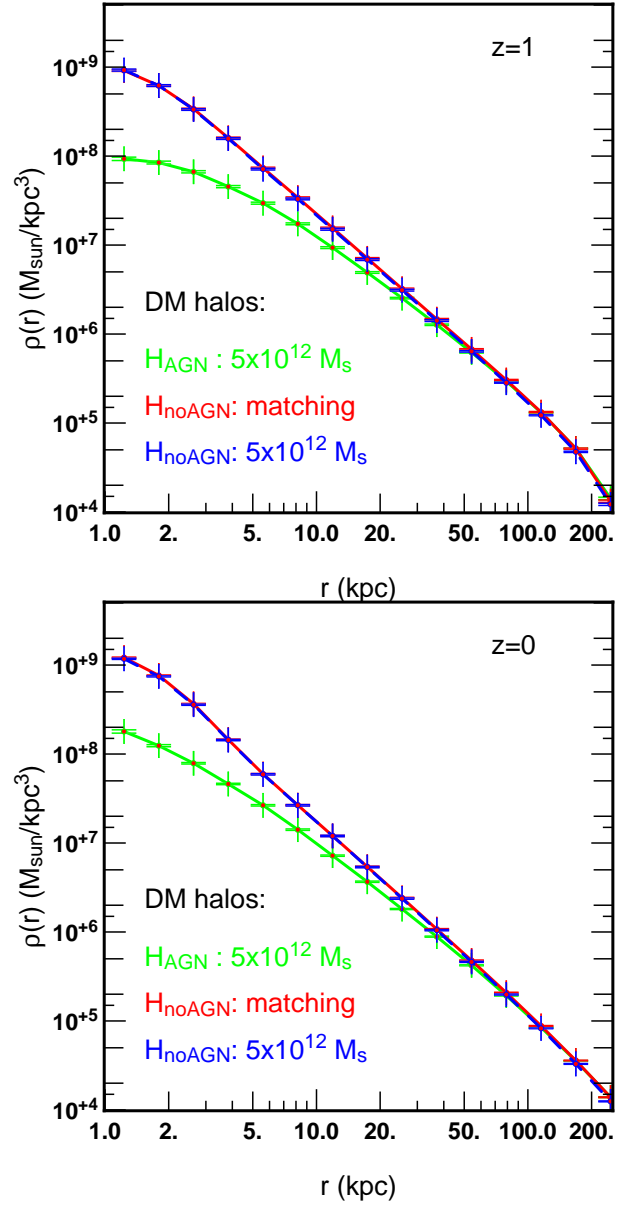


Figure 13. Mean density profiles of dark matter haloes with a mass of $5 \times 10^{12} M_{\odot}$ at $z = 1$ (upper panel) and $z = 0$ (lower panel) and extracted from the HORIZON-AGN (green) or HORIZON-NOAGN (blue) simulations. The DM density profile of matched haloes is plotted in red. Since AGN feedback does not affect the virial mass of DM haloes, the red and blue profiles sample the same population of haloes and are therefore indistinguishable.

tening). From very high redshift to $z \sim 3$, ρ_{AGN} becomes steeper than ρ_{DM} due to adiabatic contraction induced by early galaxy formation in the center of the host dark matter haloes. From $z \sim 3$ down to $z \sim 1.6$, ρ_{AGN} is noticeably flattened by AGN activity which is high (quasar mode). From $z \sim 1.6$ to the present time, ρ_{AGN} steepens again (“cusp regeneration”) as AGN activity considerably reduces.

- The gaps between ρ_{AGN} , ρ_{noAGN} and ρ_{DM} are also evolving with time. At high redshift, ρ_{AGN} and ρ_{noAGN} tend to be much steeper than ρ_{DM} due to rapid galaxy formation. Until $z \sim 1.6$, the flattening of ρ_{AGN} tends to increase the gap with ρ_{noAGN} and conversely decrease the gap with ρ_{DM} .

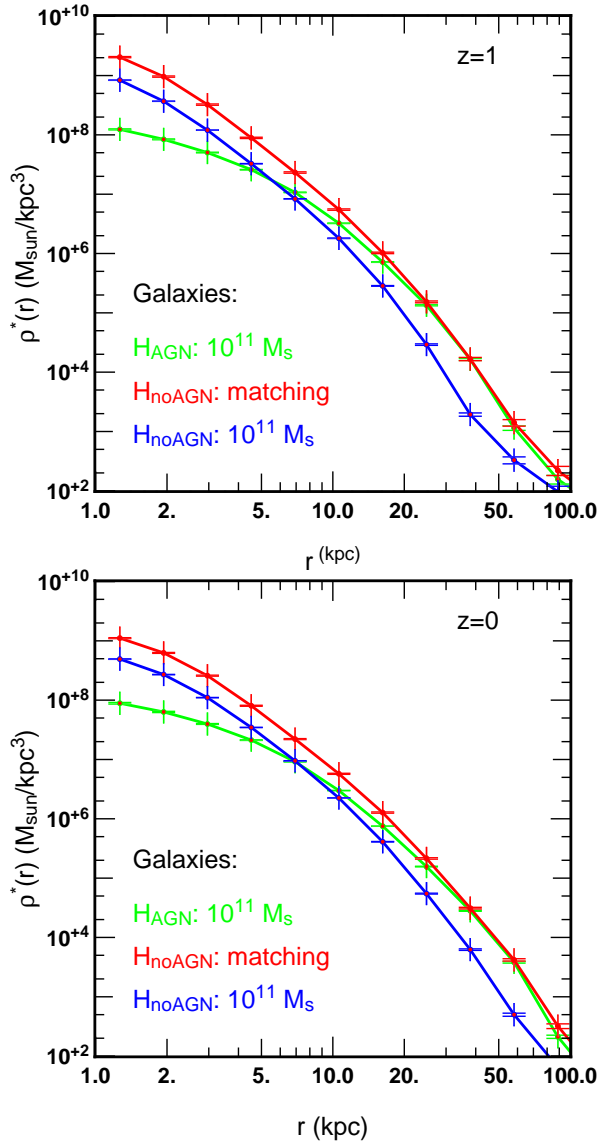


Figure 14. Mean stellar density profiles of galaxies with a mass of $10^{11} M_{\odot}$ at $z = 1$ (upper panel) and $z = 0$ (lower panel) and extracted from the HORIZON-AGN (green) or HORIZON-NOAGN (blue) simulations. The stellar density profile of the matched galaxies is plotted in red. Contrary to the dark matter component, the presence of AGN feedback significantly affects the virial mass of the galaxies. In this case, the red and blue profiles are not derived from the same population of galaxies and are therefore very different.

Finally after $z \sim 1.6$, the phase of “cusp regeneration” leads to both a slight reduction and increase of the gap w.r.t. ρ_{noAGN} and ρ_{DM} respectively.

- AGN feedback noticeably reduces the central density in massive galaxies and efficiently flattens their inner profiles, which lead to trends more compatible with the observations of massive elliptical or cD galaxies, that exhibit very shallow slopes in the stellar surface brightness profiles within small radii (≈ 1 kpc) (Kormendy 1999; Quillen, Bower & Stritzinger 2000; Laine et al. 2003; Graham 2004; Trujillo et al. 2004; Lauer et al. 2005; Ferrarese et al. 2006; Côté et al. 2007; Kormendy et al. 2009; Graham 2013). In contrast to the

dark matter component, galaxy inner density profiles remain quite flat at low redshifts.

- At any given redshift, more massive dark matter haloes or galaxies have in general flatter central density profiles than their less massive counterparts. The impact of AGN feedback in the flattening of DM haloes/galaxies density profiles is all the more important than the objects are massive.
- Without AGN feedback, the inner density profiles of dark matter haloes and galaxies are always very steep.

The present study clearly demonstrates that the inner density profiles of dark matter haloes and galaxies are very sensitive to sub-grid physics and more specifically to AGN feedback. For instance, our model predicts a 3-phase scenario in the evolution of dark matter density profiles which is intimately associated with the strength of AGN activity via the contribution of the different accretion modes on the central BH. Indeed, as advocated by Peirani et al. (2008), repetitive cycles of gas expansion by AGN feedback and gas cooling are requested to efficiently flatten the dark matter profiles. If the AGN activity progressively decreases, this proposed mechanism becomes less efficient at counterbalancing the DM adiabatic contraction and at keeping the DM density profiles flat. Furthermore, we also found that the radio mode tends to be the dominant mode after $z \sim 2$, which renders the expansion phase of the gas more difficult. Future accurate observations will allow to confirm these theoretical predictions, but, above all, will help constraining AGN models. One complication may arise when trying to probe the distribution of the DM component. If one assumes that the stellar mass distribution will trace that of the DM then high resolution observations of large samples of massive galaxies across a large redshift range are requested. This could be done using EUCLID in the redshift range $z < 1$ and JWST in the redshift range $1 < z < 4$.

We mainly focused on the inner part of dark matter haloes density profiles where clear differences can be seen between the different simulations. Conversely, for a given mass sample, the density profiles of H_{AGN} haloes and their matching H_{noAGN} and H_{DM} haloes converge and become identical at distances $r > 10 - 20$ kpc, which suggests that these outer regions are not affected by baryons and AGN feedback. However, previous works indicate that AGN feedback is also expected to produce effect on larger scales. For instance, AGN feedback is essential to produce massive galaxies that resemble ellipticals. Without BH activity, massive galaxies are disc-like with kinematics dominated by rotational support (see Dubois et al., 2013; Dubois et al. 2016). At even larger scales, Suto et al. (2016) have recently examined the asphericity of galaxy clusters using the projected axis ratios of X-ray surface brightness, star, and dark matter distributions of the most massive haloes ($M_{200} > 5 \times 10^{13} M_{\odot}$) extracted from HORIZON-AGN, HORIZON-NOAGN and HORIZON-DM. They found that the baryonic physics and especially AGN feedback can significantly affect the asphericity of dark matter distribution even beyond the central region, approximately up to the half of the virial radius. AGN feedback seems therefore an indispensable ingredient for the formation of massive dark matter haloes and galaxies.

In a companion paper, we will investigate the effect of AGN feedback on the total (DM + stars) density slope of massive early-type galaxies estimated at the effective radius.

Acknowledgements

We warmly thank Y.Suto and T.Nishimichi for interesting discussions. S.P. acknowledges support from the Japan Society for the Promotion of Science (JSPS long-term invitation fellowship). This work was granted access to the HPC resources of CINES under the allocations 2013047012, 2014047012 and 2015047012 made by GENCI and has made use of the Horizon cluster hosted by the Institut d'Astrophysique de Paris on which the simulation was post-processed. This work was carried out within the framework of the Horizon project (<http://www.projet-horizon.fr>) and is partially supported by the grants ANR-13-BS05-0005 of the French Agence Nationale de la Recherche. The research of J.D. is supported by Adrian Beecroft and STFC.

REFERENCES

- Abadi, M. G., Navarro, J. F., Fardal, M., Babul, A., & Steinmetz, M. 2010, *MNRAS*, 407, 435
- Ahn, K., & Shapiro, P. R. 2005, *MNRAS*, 363, 1092
- Aubert, D., Pichon, C., & Colombi, S. 2004, *MNRAS*, 352, 376
- Blumenthal, G. R., Faber, S. M., Flores, R., & Primack, J. R. 1986, *ApJ*, 301, 27
- Bode, P., Ostriker, J. P., & Turok, N. 2001, *ApJ*, 556, 93
- Bournaud, F., Jog, C. J., & Combes, F. 2007, *A&A*, 476, 1179
- Bundy, K., Bershad, M. A., Law, D. R., et al. 2015, *ApJ*, 798, 7
- Burkert, A. 2000, *ApJ*, 534, L143
- Chan, T. K., Kereš, D., Oñorbe, J., et al. 2015, *MNRAS*, 454, 2981
- Cheung, E., Bundy, K., Cappellari, M., et al. 2016, *Nature*, 533, 504
- Cole, D. R., Dehnen, W., & Wilkinson, M. I. 2011, *MNRAS*, 416, 1118
- Colín, P., Avila-Reese, V., & Valenzuela, O. 2000, *ApJ*, 542, 622
- Côté, P., Ferrarese, L., Jordán, A., et al. 2007, *ApJ*, 671, 1456
- Davé, R., Spergel, D. N., Steinhardt, P. J., & Wandelt, B. D. 2001, *ApJ*, 547, 574
- de Blok W. J. G., McGaugh S. S., Bosma A. & Rubin V. C., 2001, *ApJ* 552, L23
- de Blok, W. J. G., Walter, F., Brinks, E., et al. 2008, *AJ*, 136, 2648-2719
- Del Popolo, A. 2009, *ApJ*, 698, 2093
- Del Popolo, A., & Pace, F. 2016, *Ap&SS*, 361, 162
- Di Cintio, A., Brook, C. B., Macciò, A. V., et al. 2014, *MNRAS*, 437, 415
- Dubois, Y., Devriendt, J., Slyz, A., & Teyssier, R. 2010, *MNRAS*, 409, 985
- Dubois, Y., Devriendt, J., Slyz, A., & Teyssier, R. 2012, *MNRAS*, 420, 2662
- Dubois, Y., Gavazzi, R., Peirani, S., & Silk, J. 2013, *MNRAS*, 433, 3297
- Dubois, Y., Pichon, C., Welker, C., et al. 2014, *MNRAS*, 444, 1453
- Dubois, Y., Peirani, S., Pichon, C., et al. 2016, *MNRAS*, 463, 3948
- Duffy, A. R., Schaye, J., Kay, S. T., et al. 2010, *MNRAS*, 405, 2161
- Dutton, A. A., & Treu, T. 2014, *MNRAS*, 438, 3594
- Elbert, O. D., Bullock, J. S., Garrison-Kimmel, S., et al. 2015, *MNRAS*, 453, 29
- El-Zant, A., Shlosman, I., & Hoffman, Y. 2001, *ApJ*, 560, 636
- El-Zant, A. A., Hoffman, Y., Primack, J., Combes, F., & Shlosman, I. 2004, *ApJ*, 607, L75
- El-Zant, A. A., Freundlich, J., & Combes, F. 2016, *MNRAS*, 461, 1745
- Faber, S. M., Tremaine, S., Ajhar, E. A., et al. 1997, *AJ*, 114, 1771
- Ferrarese, L., Côté, P., Jordán, A., et al. 2006, *ApJS*, 164, 334
- Gentile, G., Salucci, P., Klein, U., Vergani, D., & Kalberla, P. 2004, *MNRAS*, 351, 903
- Gnedin, O. Y., & Zhao, H. 2002, *MNRAS*, 333, 299
- Gnedin, O. Y., Kravtsov, A. V., Klypin, A. A., & Nagai, D. 2004, *ApJ*, 616, 16
- Goerdt, T., Moore, B., Read, J. I., Stadel, J., & Zemp, M. 2006, *MNRAS*, 368, 1073
- Governato, F., Zolotov, A., Pontzen, A., et al. 2012, *MNRAS*, 422, 1231
- Graham, A. W. 2004, *ApJ*, 613, L33
- Graham, A. W. 2013, *Planets, Stars and Stellar Systems. Volume 6: Extragalactic Astronomy and Cosmology*, 6, 91
- Gustafsson, M., Fairbairn, M., & Sommer-Larsen, J. 2006, *Phys. Rev. D*, 74, 123522
- Haardt, F., & Madau, P. 1996, *ApJ*, 461, 20
- Holley-Bockelmann, K., Weinberg, M., & Katz, N. 2005, *MNRAS*, 363, 991
- Hopkins, P. F., Richards, G. T., & Hernquist, L. 2007, *ApJ*, 654, 731
- Jardel, J. R., & Sellwood, J. A. 2009, *ApJ*, 691, 1300
- Jing, Y. P., & Suto, Y. 2000, *ApJ*, 529, L69
- Kaviraj, S., Laigle, C., Kimm, T., et al. 2016, *arXiv:1605.09379*
- Khochfar, S., & Silk, J. 2006, *ApJ*, 648, L21
- Kimm, T., Kaviraj, S., Devriendt, J. E. G., et al. 2012, *MNRAS*, 425, L96
- Klypin, A., Yepes, G., Gottlöber, S., Prada, F., & Heß, S. 2016, *MNRAS*, 457, 4340
- Kochanek, C. S., & White, M. 2000, *ApJ*, 543, 514
- Kormendy, J. 1999, *Galaxy Dynamics - A Rutgers Symposium*, 182, Kormendy, J., Fisher, D. B., Cornell, M. E., & Bender, R. 2009, *ApJS*, 182, 216
- Lackner, C. N., & Ostriker, J. P. 2010, *ApJ*, 712, 88
- Laine, S., van der Marel, R. P., Lauer, T. R., et al. 2003, *AJ*, 125, 478
- Lauer, T. R., Faber, S. M., Gebhardt, K., et al. 2005, *AJ*, 129, 2138
- Leonard, A., Goldberg, D. M., Haaga, J. L., & Massey, R. 2007, *ApJ*, 666, 51
- Limousin, M., Richard, J., Jullo, E., et al. 2007, *ApJ*, 668, 643
- Lin, H. W., & Loeb, A. 2016, *J. Cosmology Astropart. Phys.*, 3, 009
- Lovell, M. R., Eke, V., Frenk, C. S., et al. 2012, *MNRAS*, 420, 2318
- Macciò, A. V., Stinson, G., Brook, C. B., et al. 2012, *ApJ*, 744, L9
- Macciò, A. V., Mainini, R., Penzo, C., & Bonometto, S. A. 2015, *MNRAS*, 453, 1371
- Marsh, D. J. E., & Pop, A.-R. 2015, *MNRAS*, 451, 2479
- Martizzi, D., Teyssier, R., Moore, B., & Wentz, T. 2012, *MNRAS*, 422, 3081
- Martizzi, D., Teyssier, R., & Moore, B. 2013, *MNRAS*, 432, 1947
- Mashchenko, S., Couchman, H. M. P., & Wadsley, J. 2006, *Nature*, 442, 539
- Mashchenko, S., Wadsley, J., & Couchman, H. M. P. 2008, *Science*, 319, 174
- Mazzalay, X., Thomas, J., Saglia, R. P., et al. 2016, *MNRAS*, 462, 2847
- Merritt, D. et al., 2004, *ApJ*, 607, L9
- Merritt, D., Graham, A. W., Moore, B., Diemand, J., & Terzić, B. 2006, *AJ*, 132, 2685
- Moore, B., Governato, F., Quinn, T., Stadel, J., & Lake, G. 1998, *ApJ*, 499, L5
- Naab, T., Johansson, P. H., & Ostriker, J. P. 2009, *ApJ*, 699, L178
- Navarro, J. F., Frenk, C. S., & White, S. D. M. 1996a, *ApJ*, 462, 563
- Navarro, J. F., Eke, V. R., & Frenk, C. S. 1996b, *MNRAS*, 283, L72
- Navarro, J. F., Frenk, C. S., & White, S. D. M. 1997, *ApJ*, 490, 493
- Navarro, J. F., Ludlow, A., Springel, V., et al. 2010, *MNRAS*, 402, 21
- Newman, A. B., Treu, T., Ellis, R. S., et al. 2009, *ApJ*, 706, 1078
- Newman, A. B., Treu, T., Ellis, R. S., & Sand, D. J. 2011, *ApJ*, 728, L39
- Newman, A. B., Treu, T., Ellis, R. S., & Sand, D. J. 2013, *ApJ*, 765, 25
- Ogiya, G., & Mori, M. 2011, *ApJ*, 736, L2
- Ogiya, G., & Mori, M. 2014, *ApJ*, 793, 46
- Oh, S.-H., de Blok, W. J. G., Brinks, E., Walter, F., & Kennicutt, R. C., Jr. 2011, *AJ*, 141, 193

- Oñorbe, J., Boylan-Kolchin, M., Bullock, J. S., et al. 2015, *MNRAS*, 454, 2092
- Oser, L., Ostriker, J. P., Naab, T., Johansson, P. H., & Burkert, A. 2010, *ApJ*, 725, 2312
- Oser, L., Naab, T., Ostriker, J. P., & Johansson, P. H. 2012, *ApJ*, 744, 63
- Palunas, P., & Williams, T. B. 2000, *AJ*, 120, 2884
- Pedrosa, S., Tissera, P. B., & Scannapieco, C. 2010, *MNRAS*, 402, 776
- Peirani, S., Kay, S., & Silk, J. 2008, *A&A*, 479, 123
- Peirani, S., Crockett, R. M., Geen, S., et al. 2010, *MNRAS*, 405, 2327
- Pontzen, A., & Governato, F. 2012, *MNRAS*, 421, 3464
- Power, C., Navarro, J. F., Jenkins, A., et al. 2003, *MNRAS*, 338, 14
- Quillen, A. C., Bower, G. A., & Stritzinger, M. 2000, *ApJS*, 128, 85
- Read, J. I., & Gilmore, G. 2005, *MNRAS*, 356, 107
- Richtler, T., Salinas, R., Misgeld, I., et al. 2011, *A&A*, 531, A119
- Rodríguez-Gomez, V., Pillepich, A., Sales, L. V., et al. 2016, *MNRAS*, 458, 2371
- Romano-Díaz, E., Shlosman, I., Hoffman, Y., & Heller, C. 2008, *ApJ*, 685, L105
- Salucci, P., & Burkert, A. 2000, *ApJ*, 537, L9
- Sand, D. J., Treu, T., Smith, G. P., & Ellis, R. S. 2004, *ApJ*, 604, 88
- Sand, D. J., Treu, T., Ellis, R. S., Smith, G. P., & Kneib, J.-P. 2008, *ApJ*, 674, 711-727
- Sellwood, J. A. 2008, *ApJ*, 679, 379-396
- Shankar, F., Weinberg, D. H., & Miralda-Escudé, J. 2009, *ApJ*, 690, 20
- Shankar, F., Marulli, F., Bernardi, M., et al. 2013, *MNRAS*, 428, 109
- Spekkens, K., Giovanelli, R., & Haynes, M. P. 2005, *AJ*, 129, 2119
- Spergel, D. N., & Steinhardt, P. J. 2000, *Physical Review Letters*, 84, 3760
- Stadel, J., Potter, D., Moore, B., et al. 2009, *MNRAS*, 398, L21
- Sutherland, R. S., & Dopita, M. A. 1993, *ApJS*, 88, 253
- Suto, D., Peirani, S., Dubois, Y., et al. 2016, arXiv:1611.05192
- Swaters, R. A., Madore, B. F., van den Bosch, F. C., & Balcells, M. 2003, *ApJ*, 583, 732
- Teyssier, R. 2002, *A&A*, 385, 337
- Teyssier, R., Moore, B., Martizzi, D., Dubois, Y., & Mayer, L. 2011, *MNRAS*, 414, 195
- Teyssier, R., Pontzen, A., Dubois, Y., & Read, J. I. 2013, *MNRAS*, 429, 3068
- Thomas, J., Saglia, R. P., Bender, R., Erwin, P., & Fabricius, M. 2014, *ApJ*, 782, 39
- Tissera, P. B., White, S. D. M., Pedrosa, S., & Scannapieco, C. 2010, *MNRAS*, 406, 922
- Tollet, E., Macciò, A. V., Dutton, A. A., et al. 2016, *MNRAS*, 456, 3542
- Tonini, C., Lapi, A., & Salucci, P. 2006, *ApJ*, 649, 591
- Trujillo, I., Erwin, P., Asensio Ramos, A., & Graham, A. W. 2004, *AJ*, 127, 1917
- Tweed, D., Devriendt, J., Blaizot, J., Colombi, S., & Slyz, A. 2009, *A&A*, 506, 647
- Ueda, Y., Akiyama, M., Hasinger, G., Miyaji, T., & Watson, M. G. 2014, *ApJ*, 786, 104
- Umetsu, K., Takada, M., & Broadhurst, T. 2007, *Modern Physics Letters A*, 22, 2099
- Vogelsberger, M., Zavala, J., Simpson, C., & Jenkins, A. 2014, *MNRAS*, 444, 3684
- Volonteri, M., Dubois, Y., Pichon, C., & Devriendt, J. 2016, *MNRAS*, 460, 2979
- Walter, F., Brinks, E., de Blok, W. J. G., et al. 2008, *AJ*, 136, 2563-2647
- Walker, M. G., & Peñarrubia, J. 2011, *ApJ*, 742, 20
- Weinberg, M. D., & Katz, N. 2002, *ApJ*, 580, 627
- Weinberger, R., Springel, V., Hernquist, L., et al. 2016, arXiv:1607.03486
- Welker, C., Dubois, Y., Devriendt, J., et al. 2015, arXiv:1502.05053
- Yoshida, N., Springel, V., White, S. D. M., & Tormen, G. 2000, *ApJ*, 535, L103
- Zitrin, A., Fabris, A., Merten, J., et al. 2015, *ApJ*, 801, 44